

Adaptive Stochastic Morphology Simulation and Mesh Generation of High-Quality 3D Particulate Composite Microstructures with Complex Surface Texture

Junjie Huang^{a,*}, Fangqian Deng^b, Lingfei Liu^a, Jianqiao Ye^c

^aCollege of Transportation, Architecture and Civil Engineering, Foshan University, Foshan, Guangdong Province 528000, China

^bSchool of Civil Engineering, Wuhan University, Wuhan, Hubei Province 430072, China

^cDepartment of Engineering, Lancaster University, Lancaster LA1 4YW, UK

Abstract

Particulate composite materials have a broad range of potential applications in engineering and other disciplines. Accurate modeling of their microstructures and fast generation of the finite element meshes play a vital role in investigating many micromechanical phenomena and improving understanding of the underlying failure mechanisms. Due to the exceedingly intricate multiscale internal structures that they possess, the modeling and meshing of their microstructures still remain difficult in general. In this work, we present a computational framework and methodology for the representation, simulation, and mesh generation of 3D stochastic microstructures of particulate composites. Towards this goal, we propose a multi-level multiscale scheme that allows for capturing the multiscale structures of particulate composite materials at both the coarse and fine scales. A bridging scale approach based on heat kernel smoothing is also presented to seamlessly link the coarse and fine scales. In addition to the microstructural modeling of particulate composite materials, we also develop an adaptive curvature-based surface and volume mesh generation algorithm for particulate composite microstructures with complex surface texture. Following the implementation of the morphology and mesh generation algorithm, a series of numerical examples are presented to demonstrate the capability and potential of the proposed method.

Keywords: Particulate Composite Materials, Microstructure, Surface Texture, Heat Kernel Smoothing

1. Introduction

Particulate composites are composed of particles that are embedded in a matrix material. Typical examples of particulate composites include cementitious composites, metal matrix composites, and ceramic matrix composites. Particulate composites are ubiquitous in many engineering applications. For instance, particulate composites play

*Corresponding author

Email address: jnjhuang@whu.edu.cn (Junjie Huang)

1
2
3 an important part in bio-implants, magnets, and dental fillings. Furthermore, particulate composites are also
4
5 involved in recent applications such as circuit boards with conductive composites and soft actuators with stretchable
6
7 piezoelectrical composites. In particulate composites, the matrix material serves as the structural support, while
8
9 the particulate inclusions are added to the matrix to improve the material properties including strength, thermal
10
11 resistivity, magnetic permeability, and electrical conductivity. Through adjusting the proportions of the particles and
12
13 the matrix material, particulate composites are capable of offering improved and tailored printability, functionality,
14
15 and manufacturing flexibility.
16

17
18 In unlocking the tremendous potential of particulate composite materials as well as analyzing the complex
19
20 micromechanical behaviors that they exhibit, a critical step is the accurate simulation of their microstructural
21
22 geometries as well as the generation of the corresponding finite element meshes. In this context, a variety of
23
24 numerical techniques have been conceived to simulate the random microstructures of particulate composites. Along
25
26 this line, simplified approaches for the modeling of geo-microstructures have been developed in a number of research
27
28 works (e.g., [1–13]). In addition, more advanced and sophisticated modeling approaches have also been reported
29
30 (e.g., [14–30]). It is however noted that, in the aforementioned studies, interest has been placed in the simulation
31
32 of the coarse-scale microstructures. Rarely, the more complex fine-scale microstructures, i.e., the surface texture,
33
34 are considered in the simulation procedure. Apparently, a more realistic approach is needed to capture the complex
35
36 morphological and topographical details of the fine-scale microstructures.
37

38
39 Parallel to the development of computational methods for the morphology modeling of realistic particulate
40
41 composite microstructures, diverse mesh generation techniques have also been developed. In the context of surface
42
43 mesh generation procedures, two major techniques exist, i.e., mesh adaptation schemes (e.g., [31–33]) and surface
44
45 parametrization methods (e.g., [34–40]). A plethora of volume mesh generation schemes have also been proposed in
46
47 the literature (e.g., [41–46]). It should be however noted that due to the extremely sophisticated geometric shape
48
49 and surface texture of particulate composites, constructing surface and volume meshes of particulate composite
50
51 microstructures can be challenging and time-consuming, which has placed increasing demands on developing more
52
53 efficient and robust mesh generation algorithms.
54

55
56 In this work, we propose a numerical framework and methodology for the morphology simulation and mesh
57
58 generation of high-quality 3D particulate composite microstructures with complex surface texture. The remainder
59
60 of this paper is organized as follows. In Section 2, a computational approach is developed for multiscale simulation
61
62
63
64
65

1
2
3 of particulate composite microstructures. After that, Section 3 proposes a numerical procedure for the mesh
4
5 generation of particulate composite microstructures. Following Section 3, Section 4 discusses the key issues in the
6
7 implementation of the proposed mesh generation procedure. On the basis of Sections 2-4, numerical examples are
8
9 then provided to illustrate the proposed algorithm. In closure, Section 6 presents a summary of the conclusions
10
11 drawn from this research work and the recommendations for future research.
12
13
14

15 **2. Morphology Generation of Particulate Composite Microstructures**

16 *2.1. Multiscale Simulation of Microstructural Inclusions of Particulate Composites*

17
18
19 As shown in Figure 1, we exploit a multi-level multiscale approach to simulate the microstructural inclusions of
20
21 particulate composites. In particular, the coarse-scale microstructure is represented by stationary Gaussian random
22
23 fields, while the fine-scale microstructure is described by fractional Brownian random fields. A computational
24
25 scheme based on heat kernel smoothing is proposed to ensure the smooth transition across different scales. As
26
27 exhibited in Figure 1, in addition to the aforementioned multiscale approach, we also adopt a multi-level scheme for
28
29 the representation of the microstructure of the particulate inclusion. At the first level, the microstructural inclusion
30
31 is represented by a surface. At the second level, the microstructural inclusion is described by a triangular mesh. At
32
33 the third level, the inclusion is characterized by a point cloud. We adopt such a continuous-discrete representation
34
35 scheme because it will be useful in the subsequent surface and volume mesh generation process. Additionally, this
36
37 representation scheme provides a natural way of simulating microstructures with both smooth and sharp features.
38
39
40

41 *2.1.1. Simulation of the Coarse-scale Microstructures of Particulate Inclusions*

42
43
44 To achieve fast generation of the coarse-scale microstructures of particulate inclusions, we adopt the approach
45
46 proposed by Huang and Peng [22] and consider a real-valued two dimensional stationary Gaussian random field
47
48 $F(\mathbf{x})$ with zero mean and the following exponential stationary covariance (see, for example, [22, 47, 48])
49
50

$$51 \quad c(\mathbf{x}) = e^{-|x_1|/\beta_1 - |x_2|/\beta_2} \quad (1)$$

52
53 in which β_1 and β_2 are constant.
54
55

56 After that, we construct a 2D rectangular grid over $[0, \pi] \times [0, 2\pi]$, i.e.,
57
58

$$59 \quad D = \left\{ \mathbf{x} = (i\Delta x_1, j\Delta x_2)^T, i = 0, \dots, n_1 - 1, j = 0, \dots, n_2 - 1 \right\} \quad (2)$$

60
61 in which the spacings are set to be uniform in both directions with $\Delta x_1 = \pi/(n_1 - 1)$ and $\Delta x_2 = 2\pi/(n_2 - 1)$.
62
63
64
65

As a result, a zero-mean stationary Gaussian field associated with the covariance function given in Equation 1 on D is reduced to sampling Gaussian random field $F(\mathbf{x})$ on D . Suppose that the resulting covariance matrix for the Gaussian random field $F(\mathbf{x})$ is M , the next step is to generate samples from $N(\mathbf{0}, M)$, i.e.,

$$\mathbf{F} = [F(\mathbf{x}_0), F(\mathbf{x}_1), \dots, F(\mathbf{x}_{N-1})]^T \sim N(\mathbf{0}, M) \quad (3)$$

where $N = n_1 \times n_2$.

After straightforward manipulations, it can be shown that the covariance matrix \hat{M} for the stationary Gaussian field F sampled on D is a symmetric Block Circulant with Circulant Blocks (BCCB) matrix of the form

$$\hat{M} = \begin{pmatrix} \hat{M}_0 & \hat{M}_{-1} & \cdots & \hat{M}_{1-n_2} & \hat{\mathbf{0}} & \hat{M}_{n_2-1} & \cdots & \hat{M}_1 \\ \hat{M}_1 & \hat{M}_0 & \ddots & \ddots & \ddots & \ddots & \ddots & \ddots \\ \vdots & \ddots \\ \hat{M}_{n_2-1} & \ddots \\ \hat{\mathbf{0}} & \hat{M}_{n_2-1} & \ddots & \ddots & \ddots & \ddots & \ddots & \ddots \\ \hat{M}_{1-n_2} & \hat{\mathbf{0}} & \ddots & \ddots & \ddots & \ddots & \ddots & \ddots \\ \vdots & \ddots & \ddots & \ddots & \ddots & \ddots & \ddots & \hat{M}_{-1} \\ \hat{M}_{-1} & \hat{M}_{-2} & \ddots & \ddots & \ddots & \ddots & \hat{M}_1 & \hat{M}_0 \end{pmatrix} \in \mathbb{R}^{4N \times 4N} \quad (4)$$

in which $\hat{\mathbf{0}}$ is the $2n_1 \times 2n_1$ zero matrix; and \hat{M}_k is the circulant matrix expanded from the Toeplitz matrix M_k using the following reduced form

$$M_k = [\mathbf{m}_{1-n_1}, \dots, \mathbf{m}_{-1}, \mathbf{m}_0, \mathbf{m}_1, \dots, \mathbf{m}_{n_1-1}]^T \in \mathbb{R}^{2n_1-1} \quad (5)$$

Similar to the Toeplitz matrix M_k , the BCCB matrix \hat{M} in Equation 4 can also be represented using its reduced form

$$\hat{M} = [\hat{\mathbf{m}}_0, \hat{\mathbf{m}}_1, \dots, \hat{\mathbf{m}}_{n_2-1}, \hat{\mathbf{0}}, \hat{\mathbf{m}}_{1-n_2}, \dots, \hat{\mathbf{m}}_{-1}]^T \in \mathbb{R}^{2n_1 \times 2n_2} \quad (6)$$

With the reduced form given in Equation 6, the BCCB covariance matrix \hat{M} can be further decomposed as

$$\hat{M} = F^* \hat{\Lambda} F \quad (7)$$

where $\hat{\Lambda}$ denotes the diagonal matrix with diagonal containing the eigenvalues of \hat{M} ; and F represents the 2D Fourier matrix.

The eigenvalues of \hat{M} can then be computed using the diagonal matrix $\hat{\Lambda}$ and the 2D Fourier matrix F

$$W = F\hat{\Lambda}^{1/2}\eta, \quad \eta \sim CN(0, 2I_{2N'}). \quad (8)$$

where $N' = 2N$; and CN denotes the complex Gaussian distribution.

It follows from Equation 8 that the real and imaginary parts of \hat{W} result in two independent samples. Figure 2 shows the coarse-scale granular microstructure of a particulate inclusion generated using the approach presented in Section 2.1.1.

2.1.2. Simulation of the Fine-scale Microstructures of Particulate Inclusions

As shown in Figure 3a, a simple approach to simulate the fine-scale surface texture of the particulate inclusion is to add random noise to the coarse-scale microstructure. In order to represent the fine-scale microstructure in a more realistic manner, as shown in Figure 3b, the fractional Brownian random field is employed to simulate the more complex surface texture of the particulate microstructure at the fine scale, which is based on the approach proposed by Huang and Peng [22].

The fractional Brownian random field $B(\mathbf{x})$ is a Gaussian random field characterized by a zero mean function and the following nonstationary covariance function (see, for example, [22, 49, 50])

$$\text{cov}(B(\mathbf{x}), B(\mathbf{y})) = \|x\|^\mu + \|y\|^\mu - \|x - y\|^\mu \quad (9)$$

where $H = \mu/2$ is the Hurst parameter.

To generate the aforementioned Gaussian random field, we first simulate a stationary Gaussian random field over $[0, \pi] \times [0, 2\pi]$ with the following covariance function

$$\text{cov}(\bar{B}(\mathbf{x}), \bar{B}(\mathbf{y})) = c_0 + c_2\|x - y\|^2 - \|x - y\|^\mu \quad (10)$$

where c_0 and c_2 are constant.

Then, we modify the simulated random field in the following way

$$\tilde{B}(x) = \bar{B}(x) - \bar{B}(0) + \sqrt{2c_2}x^T Z, \quad Z = (Z_1, Z_2)^T, \quad Z_1, Z_2 \sim N(\mathbf{0}, I) \quad (11)$$

It can be shown that the covariance of the aforementioned Gaussian field $\text{cov}(\tilde{B}(\mathbf{x}), \tilde{B}(\mathbf{y}))$ is equivalent to the nonstationary covariance of the fractional Brownian field $\text{cov}(B(\mathbf{x}), B(\mathbf{y}))$ [22, 50].

To illustrate the generation of fine-scale microstructures using the fractional Brownian random fields, Figure 3b shows the generated fine-scale microstructure that corresponds to the coarse-scale particulate inclusion of Figure 2.

1
2
3 *2.1.3. Coupling of the Coarse-scale and Fine-scale Microstructures of Particulate Inclusions*
4

5 To bridge the gap between coarse-scale and fine-scale microstructures, as illustrated in Figure 4, we present a
6 multiscale heat kernel smoothing scheme that allows for smooth transition between the coarse scale and the fine
7 scale, which can be formulated as a Cauchy problem, i.e.,
8
9

$$10 \quad \partial_t g + \mathcal{L}g = 0, \quad g(p, t = 0) = f(p) \quad (12)$$

11 where $f(p)$ is the initial functional data that can be randomly simulated as
12
13

$$14 \quad f(p) = \nu(p) + \epsilon(p) \quad (13)$$

15 where ν denotes the unknown signal; ϵ signifies the random noise characterized by a mean zero Gaussian random
16 field; \mathcal{L} is a self-adjoint linear partial differential operator with the following property
17
18

$$19 \quad \langle g_1, \mathcal{L}g_2 \rangle = \langle \mathcal{L}g_1, g_2 \rangle \quad (14)$$

20 for all $g_1, g_2 \in L^2(\mathcal{M})$, in which \mathcal{M} denotes a compact differential manifold and $\langle g_1, g_2 \rangle$ stands for the inner product
21
22

$$23 \quad \langle g_1, g_2 \rangle = \int_{\mathcal{M}} g_1(p)g_2(p)d\mu(p) \quad (15)$$

24 The eigenvalues λ_j and eigenfunctions ψ_j of \mathcal{L} can be acquired by solving
25
26

$$27 \quad \mathcal{L}\psi_j = \lambda_j\psi_j \quad (16)$$

28 Upon mapping \mathcal{M} to a unit sphere S^2 , the operator \mathcal{L} becomes the spherical Laplacian operator, i.e., $\mathcal{L} = \Delta$.
29
30

31 As a result, the Cauchy problem is reduced to the following isotropic heat diffusion equation
32
33

$$34 \quad \frac{\partial g}{\partial t} = \Delta g, \quad g(p, t = 0) = f(p) \quad (17)$$

35 where Δ is the spherical Laplacian operator given by
36
37

$$38 \quad \Delta = \frac{1}{\sin\theta} \frac{\partial}{\partial\theta} \left(\sin\theta \frac{\partial}{\partial\theta} \right) + \frac{1}{\sin^2\theta} \frac{\partial^2}{\partial\phi^2} \quad (18)$$

39 Correspondingly, the eigenvalues and eigenfunctions of the spherical Laplacian Δ are given by
40
41

$$42 \quad \Delta Y_{lm} = \lambda_l Y_{lm} \quad (19)$$

where $\lambda_l = l(l+1)$ and $Y_{lm}(-l \leq m \leq l)$ are termed as the spherical harmonic of degree l and order m that take the form

$$Y_{lm} = \begin{cases} c_{lm} P_l^{|m|}(\cos\theta) \sin(|m|\phi) & -l \leq m \leq l, \\ \frac{c_{lm}}{\sqrt{2}} P_l^{|m|}(\cos\theta) & m = 0, \\ c_l m P_l^{|m|}(\cos\theta) \cos(|m|\phi) & 1 \leq m \leq l, \end{cases} \quad (20)$$

in which $c_{lm} = \sqrt{\frac{(2l+1)}{2\pi} \frac{(l-|m|)!}{(l+|m|)!}}$ and P_l^m is the associated Legendre polynomials of order m .

The solution of the isotropic heat diffusion equation, i.e., Equation 17, can be constructed by using the weighted Fourier series [52–54]

$$g(p, t) = \sum_{j=0}^{\infty} b_j e^{-\lambda_j t} \psi_j(p) = \sum_{j=0}^{\infty} e^{-\lambda_j t} \langle f, \psi_j \rangle \psi_j(p) \quad (21)$$

where the coefficients $b_j = \langle f, \psi_j \rangle$ are the Fourier coefficients.

The finite truncation of the infinite weighted Fourier series leads to

$$\mathcal{F}_t^k[f](p) = \sum_{j=0}^k e^{-\lambda_j t} \langle f, \psi_j \rangle \psi_j(p) \quad (22)$$

It follows from Equations 21 and 22 that the weighted Fourier series differ from the traditional Fourier series in the exponential term $e^{-\lambda_j t}$. This exponential term, however, has advantages. More importantly, with this exponential term, the finite weighted Fourier series can be reformulated in the framework of heat kernel smoothing, which will also be utilized in the noise diffusion and mesh generation of microstructures with complex geometric shape and surface texture discussed later in Section 3. This can be shown by rewriting the finite weighted Fourier series as

$$\mathcal{F}_t^k[f](p) = \sum_{j=0}^k e^{-\lambda_j t} \psi_j(p) \int_{S^2} f(q) \psi_j(q) d\mu(q) = \int_{S^2} f(q) K_t^k(p, q) d\mu(q) \quad (23)$$

in which $K_t^k(p, q)$ is the symmetric positive definite kernel defined as

$$K_t^k(p, q) = \sum_{j=0}^k e^{-\lambda_j t} \psi_j(p) \psi_j(q) \quad (24)$$

Utilizing the eigenvalues and eigenfunctions in Equation 19, the heat kernel $K_t^k(p, q)$ can be recast as

$$K_t^k(p, q) = \sum_{l=0}^k \sum_{m=-l}^l e^{-l(l+1)t} Y_{lm}(p) Y_{lm}(q) \quad (25)$$

in which the ordered eigenvalues $\lambda_{00} \leq \lambda_{1m_1} \leq \lambda_{1m_2} \leq \dots \leq 0$ satisfy

$$\int_{S^2} K_t^k(p, q) Y_{lm}(p) d\mu(q) = \lambda_{lm} Y_{lm}(p) \quad (26)$$

1
2
3 Substituting Equation 25 into Equation 23 leads to

$$4 \quad \mathcal{F}_t^k[f](p) = \sum_{l=0}^k \sum_{m=-l}^l e^{-l(l+1)t} f_{lm} Y_{lm}(p) \quad (27)$$

7
8 where f_{lm} is the Fourier coefficient $f_{lm} = \langle f, Y_{lm} \rangle$

10 Equation 27 implies that the weighted spherical harmonics are the finite expansion of heat kernel smoothing. The
11 heat kernel smoothing technique in combination with the associated weighted spherical harmonic representation
12 scheme permits coupling of the coarse and fine scales in a smooth and gradual way. Figure 4 illustrates the
13 evolution of the coarse and fine scales of the particulate microstructures in Figures 2 and 3b realized by the heat
14 kernel smoothing technique.
15
16
17
18
19
20
21

22 *2.2. Multiscale Simulation of Representative Volume Elements of Particulate Composites*

23 In addition to the simulation of the microstructural inclusions of particulate composites, another important
24 consideration is to place the generated microstructural inclusions into the Representative Volume Element (RVE).
25 Typically, there are two major strategies for generating microstructural RVEs, i.e., the "take-and-place" approach
26 and the "divide-and-fill" approach. In the "take-and-place" approach, inclusions are first generated and then packed,
27 on a one-by-one basis, into a given RVE domain. In the packing process, the newly placed inclusions are not allowed
28 to touch any other inclusions that have been placed in the RVE box. Alternatively, the RVE can be generated by
29 the "divide-and-fill" approach. In this approach, the RVE is first divided into smaller cells. The inclusions are then
30 filled into these cells.
31
32
33
34
35
36
37
38
39
40

41 In view of the pros and cons of the two microstructural RVE generation approaches, we propose a hybrid
42 method that combines the merits of the two approaches. As shown in Figure 5, we first apply the "take-and-place"
43 approach and generate non-intersecting spheres that are randomly distributed in the RVE. By using the centers of
44 the random sphere particles as the seeds, we then use these seeds to decompose the RVE into 3D Voronoi cells. In
45 a 3D tessellated domain with N seed points, the i -th Voronoi cell can be mathematically expressed as
46
47
48
49
50
51

$$52 \quad \{R_{p_i}\} = \{x \in \mathbb{R}^3 : \|\mathbf{P}_i - \mathbf{x}\| \leq \|\mathbf{P}_j - \mathbf{x}\|, j = 1, \dots, N, j \neq i\} \quad (28)$$

53 where N is the total number of seed points; \mathbf{P}_j stands for the j -th seed point; R_{p_i} represents the cell corresponding
54 to the i -th seed point \mathbf{P}_i ; and \mathbf{x} denotes a generic point in \mathbb{R}^3 .
55
56
57
58
59

60 With the RVE divided into 3D Voronoi cells, we now proceed to place the generated microstructural inclusions
61 into the cells. As shown in Figures 6-8, to ensure that an inclusion of complex shape can be properly placed into
62
63
64
65

1
2
3 a given cell, we concoct scaling, subdivision, and fusion in the cell filling process. More specifically, in the scaling
4
5 operation, the generated inclusion is scaled with respect to its geometric center so that it can be completely fit
6
7 into the cell, which is shown in Figure 6. As shown in Figure 7, in the subdivision operation, the cell is further
8
9 subdivided into smaller cells so that the smaller microstructural inclusions can be placed into these smaller cells.
10
11 Different from scaling and subdivision, we also propose a fusion operation, which is shown in Figure 8. To perform
12
13 the fusion operation, the set of points of the inclusion that lies outside the cell is first detected and discarded. After
14
15 that, a new point cloud that combines the inclusion and the cell is formed.
16
17
18

19 **3. Mesh Generation of Particulate Composite Microstructures**

20
21

22 As mentioned earlier, particulate composite microstructures typically have a complex geometric shape and
23
24 surface texture, the mesh generation of which could be challenging and time-consuming. In this research, we
25
26 propose a two-step mesh generation procedure for meshing particulate composite microstructures. As the first
27
28 step, an initial surface mesh is generated. We then evaluate the initial surface mesh and determine if further mesh
29
30 refinement and smoothing will be needed. It is noted that the quality of the generated and smoothed surface
31
32 mesh is of paramount importance as it provides the basis for the subsequent volume mesh generation. In addition,
33
34 the random noise present in the complex fine-scale surface texture of a particulate microstructure may pose a
35
36 significant challenge to the generation of the volume mesh. Thus, special care needs to be taken during the surface
37
38 mesh generation process. To address this issue, we propose an adaptive curvature-based surface mesh generation
39
40 procedure that is based on heat kernel smoothing. On the basis of the surface mesh generated in the first step, a
41
42 3D volume mesh is then generated using the Delaunay meshing method. After that, we evaluate the quality of the
43
44 generated volume mesh using a proposed element shape quality metric to see if the generated volume mesh needs
45
46 additional local mesh refinement.
47
48
49

50 *3.1. Surface Parametrization*

51
52

53 As mentioned earlier, one of the most salient features of particulate composites is the random and complex
54
55 microstructure. Meshing such a complicated microstructure may cause substantial computational difficulties. To
56
57 address this issue, we first utilize surface parametrization to simplify the computation. In this way, the computations
58
59 are done on \mathbb{S}^2 . To achieve this goal, we consider a closed 3D microstructural surface \mathcal{M} and a surface \mathcal{N} embedded
60
61 in \mathbb{S}^2 . It is assumed that \mathcal{M} and \mathcal{N} are smooth 2-D Riemannian manifolds. The parametrization of surface \mathcal{M} is
62
63
64
65

defined through a surface map $U(x)$ as

$$x \in \mathcal{M} \subset \mathbb{R}^3 \mapsto U(x) \in \mathcal{N} \subset \mathbb{R}^2 \quad (29)$$

The map U between \mathcal{M} and \mathcal{N} is conformal if a positive scalar function g that satisfies $U * ds^2 \mathcal{M} = g * ds^2 \mathcal{N}$ exists. A number of surface parametrization methods are present in the literature (e.g., [38–40]). In this research, we adopt the approach proposed by Choi et al. [51]. Specifically, suppose that surface \mathcal{N} is a unit sphere. The spherical conformal parametrization of $U : \mathcal{M} \mapsto \mathcal{N}$ can be achieved by the solution of the following Laplace equation

$$\Delta_{\mathcal{M}}^T U = 0 \quad (30)$$

where $\Delta_{\mathcal{M}}^T U$ is the tangential component of $\Delta_{\mathcal{M}} U$ on the tangent plane of \mathcal{N} .

It is noted that because the operator $\Delta_{\mathcal{M}}^T$ is nonlinear, solving Equation 30 may be time-consuming. Instead, we can formulate the spherical parametrization problem to a planar conformal parametrization problem, i.e.,

$$\Delta_{\mathcal{M}} U = 0 \quad (31)$$

However, this may induce conformality distortions near the puncture. To overcome this, Choi et al. [51] suggested using a quasi-conformal map $\bar{U} : \mathbb{S}^2 \rightarrow \mathbb{S}^2$. The next step is to compute \bar{U} on \mathbb{R}^2 . To linearize the problem and further improve the computational efficiency, Choi et al. [51] also exploited projecting \mathbb{S} conformally onto the complex plane through the south pole stereographic projection P_S defined on a big triangle on \mathbb{C} . As a result, the parametrization is reduced to finding a quasi-conformal map $\bar{U} : \mathbb{C} \rightarrow \mathbb{C}$ with Beltrami differential $\tilde{\mu}$, where $\tilde{\mu}$ is the Beltrami differential of $(P_S \circ \phi_i)^{-1}$. The required quasi-conformal map can then be obtained by $U = P_S^{-1} \circ \bar{U} \circ P_S$. Figure 9 shows the parametrization of a cortical surface using the surface parametrization procedure adopted in the present study.

3.2. Curvature-based Surface and Volume Mesh Generation

Once the initial surface mesh is parametrized using the procedure presented in Section 3.1, we then evaluate the curvature of the surface mesh. For fast computation of the curvature, we exploit the multi-level point-based representation scheme presented in Section 2 and adopt a point-based algorithm to compute the local surface properties using sampled points in the local neighborhood of the local surface. More specifically, we consider a smooth, two-manifold boundary surface S of a 3D microstructure that is represented by a point cloud $P = \{p_i \in \mathbb{R}^3\}$. Further, we denote N_p as the set of k -nearest neighbors of a sample $p \in P$.

By using the following covariance matrix C for the local neighborhood N_p and the sample point p , the local surface properties can be computed as [55]

$$C = \begin{bmatrix} p_{i_1} - \bar{p} \\ \dots \\ p_{i_k} - \bar{p} \end{bmatrix}^T \cdot \begin{bmatrix} p_{i_1} - \bar{p} \\ \dots \\ p_{i_k} - \bar{p} \end{bmatrix}, i_j \in N_p \quad (32)$$

in which \bar{p} is the centroid of the neighbors p_{i_j} of p .

Given the following eigenvector problem

$$C \cdot v_j = \lambda_j \cdot v_j, j \in \{0, 1, 2\}, \quad (33)$$

where $\lambda_0 \leq \lambda_1 \leq \lambda_2$, it can be shown that v_0 in the plane

$$T(x) : (x - \bar{p}) \cdot v_0 = 0 \quad (34)$$

approximates the surface normal n_p at p [55].

In addition to the estimation of the normal of the surface, the eigenvalues λ_j of the covariance matrix C can also be used to estimate the surface curvature. If we denote $\lambda_0 = \min(\lambda_j)$, the variation of a point p along the surface normal n_p can be formulated as

$$\sigma_p = \frac{\lambda_0}{\lambda_0 + \lambda_1 + \lambda_2} \quad (35)$$

Pauly et al. [55] showed that this ratio reflects the change of curvature in a neighborhood centered around p and is an approximate measure of surface curvature.

Upon utilizing Equation 35, the curvature of the surface mesh can be computed. It is noted that as the point-sampled surface could be rather noisy, proper smoothing of the initial surface mesh may be needed. Additionally, as the surface mesh serves as the input for the subsequent volume mesh, the quality of the surface mesh could have a significant effect on the generation of the volume mesh. In order to evaluate the quality of the surface mesh, we propose an iterative smoothing procedure. To achieve the goal, we use the heat kernel smoothing procedure introduced earlier in Section 2.1.3 in combination with a stopping criterion based on relative curvature variance ratio. In particular, suppose that V_c^{i+1} and V_c^i are the variance of the curvature of the surface mesh after iteration

1
2
3 $i + 1$ and the variance of the curvature of the mesh after iteration i , respectively. We then compute the relative
4
5 curvature variance ratio r_c of the two meshes as follows

$$r_c = \frac{|V_c^{i+1} - V_c^i|}{|V_c^i|} \quad (36)$$

6
7
8
9
10
11 If the computed relative curvature variance ratio is high, we then smooth the surface mesh and generate an
12
13 updated surface mesh. This iterative smoothing process goes on until the computed relative curvature variance
14
15 ratio is smaller than a predefined tolerance. Once the surface mesh is obtained, Delaunay-based meshing algorithm
16
17 is then utilized to generate the volume mesh for the given surface mesh. Figure 10 illustrates the smoothing of the
18
19 cortical surface mesh that is performed using the curvature-based surface mesh generation procedure proposed in
20
21 this study. It is noted that in Figure 10a, random noise has been added to the outer cortical surface. The smoothed
22
23 cortical surface is displayed in Figures 10b-10e. The volume mesh of the smoothed cortical surface shown in Figure
24
25 10e is presented in Figure 11.

26 27 28 29 **4. Implementation Aspects**

30
31
32 In implementing the computational framework presented in Sections 2 and 3, there are a number of issues that
33
34 need particular attention. In this section, we sketch the outline that summarizes how the proposed numerical
35
36 procedure works. We also discuss the major issues in the implementation of the proposed methodology.

37 38 39 *4.1. Overview of the Implementation of the Proposed Methodology*

40
41
42 As discussed in Sections 2 and 3, the proposed methodology is basically divided into three main steps, namely
43
44 inclusion generation step, RVE generation step, and mesh generation step. As the first step, we generate the
45
46 coarse-scale and fine-scale microstructures of particulate inclusions. After that, the generated microstructures are
47
48 placed into the RVE using the proposed cell-filling method. Following the generation of the RVE microstructure,
49
50 the surface and volume meshes are then generated. For the sake of clarity, Figure 12 presents the flowchart of the
51
52 complete computational framework proposed in the present study for generating and meshing particulate composite
53
54 microstructures. The detailed steps of the proposed procedure are provided in Algorithm 1. The essential issues
55
56 concerning the implementation of the procedure are discussed shortly in the next subsection.

1
2
3 *4.2. Key Issues in the RVE Morphology and Mesh Generation Procedure*
4

5 As mentioned in Section 3, the coarse-scale and fine-scale particulate inclusions are realized by the stationary
6 Gaussian and fractional Brownian random fields, respectively, which are constructed on 2D rectangular grids. Sim-
7 ply converting the initially generated random fields on these 2D rectangular grids into 3D Cartesian or spherical
8 coordinates may not yield a naturally closed 3D surface. As a result, appropriate postprocessing of the connected
9 interface of the converted 3D surface may be needed to enforce the continuity conditions at the interface. This
10 problem could be easily resolved using the surface smoothing procedure presented in this study. Instead of taking a
11 local approach and smoothing the neighborhood area of the connected interface (e.g., [22]), we apply the proposed
12 heat kernel smoothing procedure to polish the generated particulate inclusion at a global scale. This global ap-
13 proach ensures a smoother transition across the connected interface, leading to a more natural and realistic shape.
14 Furthermore, as the initially generated surface mesh may contain noisy and sharp features, direct generation of
15 the corresponding volume mesh from the initial surface mesh may fail. Thus, noise removal and surface smoothing
16 may be needed, which is implemented in two steps. As the first step, we integrate the heat diffusion equation to
17 reduce the noise. If further surface remeshing is needed, weighted spherical harmonic smoothing is then utilized
18 to perform surface flattening, which is shown in Figure 13. In both cases mentioned earlier, an important issue
19 in performing the heat kernel smoothing operation is the construction of the Fourier coefficients $f_{lm} = \{f, Y_{lm}\}$
20 in the weighted spherical harmonic expansions, which is done via the Iterative Residual Fitting (IRF) algorithm
21 developed in [52–54].
22
23
24
25
26
27
28
29
30
31
32
33
34
35
36
37
38
39
40

41 The basic idea of the the IRF algorithm is to evaluate the Fourier coefficients iteratively by solving the problem
42 in the subspace \mathcal{H}_k , i.e.,
43

$$44 \quad \mathcal{H}_k = \left\{ \sum_{l=0}^k \sum_{m=-l}^l \beta_{lm} Y_{lm} : \beta_{lm} \in \mathbb{R} \right\} \subset L^2(S^2) \quad (37)$$

45 The subspace \mathcal{H}_k is then further decomposed as
46
47

$$48 \quad \mathcal{H}_k = \mathcal{I}_0 \oplus \mathcal{I}_1 \oplus \cdots \oplus \mathcal{I}_k \quad (38)$$

49 in which subspace \mathcal{I}_l is given by
50
51

$$52 \quad \mathcal{I}_l = \left\{ \sum_{m=-l}^l \beta_{lm} Y_{lm}(p) : \beta_{lm} \in \mathbb{R} \right\} \quad (39)$$

53 As a result, constructing the WFS Fourier coefficients is reduced to the minimization of the following problem
54
55

$$56 \quad \|f - h\|^2 = \sum_{i=1}^n \left[f(p_i) - \beta_{lm} Y_{lm}(p_i) \right]^2 \quad (40)$$

in which

$$h = \sum_{l=0}^k \sum_{m=-l}^l \beta_{lm} Y_{lm}(p) \in \mathcal{H}_k \quad (41)$$

Equation 40 can be recast in the following matrix form

$$\mathbf{f} = \mathbf{Y}\boldsymbol{\beta} \quad (42)$$

in which $\mathbf{f} = (f(p_1), \dots, f(p_n))'$, $\boldsymbol{\beta}_l = (\beta_{l,-l}, \dots, \beta_{l,l})'$, and

$$\mathbf{Y}_l = \begin{bmatrix} Y_{l,-l}(p_1) & \cdots & Y_{l,l}(p_1) \\ \vdots & \ddots & \vdots \\ Y_{l,-l}(p_n) & \cdots & Y_{l,l}(p_n) \end{bmatrix} \quad (43)$$

is a $n \times (2l + 1)$ submatrix consisting of the l -th degree spherical harmonics evaluated at each node p_i .

It follows from Equation 42 that $\boldsymbol{\beta}$ can be obtained as

$$\boldsymbol{\beta} = (\mathbf{Y}'\mathbf{Y})^{-1}\mathbf{Y}'\mathbf{f} \quad (44)$$

Instead of directly computing the Fourier coefficients $\boldsymbol{\beta}_l$, the IRF algorithm calculates $\boldsymbol{\beta}_l$ in each subspace \mathcal{I}_l using the following residual vector in an iterative fashion, i.e.,

$$\mathbf{r}_{l-1} = \mathbf{f} - \sum_{j=0}^{l-1} e^{-j(j+1)t} \mathbf{Y}_j \boldsymbol{\beta}_j \quad (45)$$

When the residual becomes reasonably small, $\boldsymbol{\beta}_l$ is then updated as

$$\boldsymbol{\beta}_l = (\mathbf{Y}_l \mathbf{Y}_l)^{-1} \mathbf{Y}_l' \mathbf{r}_{l-1} \quad (46)$$

After the particulate inclusions are generated, the next issue is to optimize their shapes and make them look more realistic. Commonly, this is accomplished by using the shape descriptor (e.g., [15, 16, 19, 20]). In this work, we adopt a hybrid numerical-experimental approach to improve the shape of the generated microstructure, which is realized by integrating the computationally generated microstructures and the experimentally determined particle shapes. To this end, a database containing real particulate inclusions of different sizes and shapes is first built. On the basis of the developed real particle database, we then use the image processing technique developed in [23] to extract the morphological information of the particles. To do this, we first convert the original color image to a black and white binary image, which is shown in Figure 14. After that, we apply the Moore-Neighbor tracing algorithm modified by Jacob's stopping criteria [56] to determine the shape profile and centroid of the particle.

Once the shape profile and centroid of the particle is obtained, we can plot the curve of the periphery radius versus the angle, which is typically coined as the signature curve $r(\theta)$. After the shape profiles and signature curves of the particle database are obtained, the morphological and spectral characteristics can then be analyzed. Specifically, for a better visualization of the shape profile and surface texture of the particle, we differentiate the signature curve and decompose the differentiated signature curve into the high-frequency part and the low-frequency part, i.e., $r'(\theta) = r'_l(\theta) + r'_h(\theta)$. The low frequency component $r'_l(\theta)$ is associated with the fundamental shape of the particle, while the high frequency component $r'_h(\theta)$ represents the surface texture of the particle. Following the work of Huang et al. [23], the total energy of the shape profile of the particle can be defined as

$$E = \int_{-\infty}^{\infty} |r'(\theta)|^2 d\theta \quad (47)$$

Similarly, the energy of the low-frequency component of the particle shape profile is given by

$$E_l = \int_{-\infty}^{\infty} |r'_l(\theta)|^2 d\theta \quad (48)$$

Accordingly, the ratio of the energy of the low-frequency component to the total energy of the shape profile can be constructed as

$$\frac{E_l}{E} = \frac{\int_{-\infty}^{\infty} |r'_l(\theta)|^2 d\theta}{\int_{-\infty}^{\infty} |r'(\theta)|^2 d\theta} \quad (49)$$

In addition to the aforementioned energy ratio, other important shape parameters including the number of significant half cycles, the ratio of the maximum periphery radius to the minimum periphery radius, standard deviation of the periphery radii can also be acquired [23]. With the shape and texture information obtained from the previous steps, the shape of a computationally generated microstructure can be optimized in the following way. As shown in Figure 15a, we first make a plane cut of the generated microstructure. Based on the intersected shape profile, we then evaluate if the computed morphological and spectral parameters of the intersected shape profile fall within the range of the established real particle database. If the generated microstructure is deemed to be unsatisfactory, the initially generated particulate microstructure is discarded. A new microstructure will be generated. The process is repeated until the newly generated microstructure is acceptable. It is worth mentioning that to generate a more realistic microstructure, instead of making one cut, multiple cuts are suggested for microstructural shape optimization, which is shown in Figure 15b.

Apart from the evaluation of the weighted Fourier coefficients and the morphological optimization of the generated microstructure, another significant consideration in the implementation of the proposed procedure is the

1
2
3 evaluation of the normal and curvature of the surface mesh of the generated microstructure. As the first step, given
4
5 a set P of n points, we use k -nearest neighbor (kNN) search to find the k closest points in P to a query point p ,
6
7 denoted as N_p . After that, the normal n can be determined by the eigenvalues and eigenvectors of the covariance
8
9 matrix C

$$10 \quad C \cdot v_j = \lambda_j \cdot v_j, j \in \{0, 1, 2\} \quad (50)$$

11
12 in which C is the covariance matrix given by

$$13 \quad C = \frac{1}{k} \sum_{i=1}^k \xi_i \cdot (p_i - \bar{p}) \cdot (p_i - \bar{p})^T \quad (51)$$

14
15 in which ξ_i is a weight coefficient; and \bar{p} denotes the centroid of N_p , i.e.,

$$16 \quad \bar{p} = \frac{1}{k} \cdot \sum_{i=1}^k p_i \quad (52)$$

17
18 As mentioned earlier in Section 3.2, if $0 \leq \lambda_0 \leq \lambda_1 \leq \lambda_2$, the normal n_p can be approximated by the eigenvector
19
20 v_0 . With λ_0 , λ_1 , and λ_2 , the surface curvature variation measure σ_p can then be computed using Equation 35.

21
22
23
24
25
26
27
28
29
30
31
32
33
34
35
36
37
38
39
40
41
42
43
44
45
46
47
48
49
50
51
52
53
54
55
56
57
58
59
60
61
62
63
64
65

A further note on the implementation of the proposed methodology is that for particulate microstructures with complex geometries, finer meshes are typically required to capture the local geometric features. A number of adaptive mesh refinement methods have been developed in the literature. Among the available refinement methods, two popular frameworks are the h-adaptive approaches (e.g., [57–59]) and the locally adaptive multi-grid (or multi-level) methods (e.g., [60–62]). In particular, the multi-grid methods have gained widespread success in physics and engineering. It is however noted that due to the very complex surface texture of the fine-scale microstructure involved in the present study, the computation with the multigrid methods could be very demanding. In this work, we take advantage of the curvature computation procedure in Section 3 and exploit a curvature-based mesh refinement strategy for optimizing the volume meshes in the critical regions. Specifically, we first identify the locations of the regions with high curvature. Meanwhile, we also compute the aspect ratios of the elements in these local areas. Based on the computed curvature and aspect ratio, we then evaluate the quality of the mesh using an element quality metric M_e that is defined as the product of the relative curvature ratio and the element aspect ratio. If the element quality metric M_e is larger than a predefined tolerance δ_e , i.e., $M_e > \delta_e$, the quality of the mesh is unsatisfactory. We then refine the mesh using the approach proposed by Shirman [63]. The mesh refinement process repeats until the element quality metric indicates a sufficiently fine mesh. A detailed study of this mesh refinement strategy will be provided in Section 5.3.

5. Numerical Applications

We have implemented the proposed numerical procedure and developed a program for the stochastic modeling and mesh generation of particulate composite microstructures. A number of numerical examples are provided to illustrate the performance and capability of the proposed procedure. To validate the proposed procedure, we also compare the proposed procedure to those obtained from existing experimental results and computational methods. In this section, the computation is performed on a Dell PC with Intel Core i7-8850H CPU (2.60 GHz) processor and 16.0 GB random-access memory. It is noted that in the examples, the volume meshes are generated using 3D tetrahedral elements.

5.1. Generation of Particulate Microstructures

In this subsection, the proposed approach is applied to generate concrete aggregate microstructure. Figure 16 presents a generated aggregate microstructure with different surface texture. Following the work of Huang and Peng [22], in generating the coarse-scale stationary Gaussian random field, the correlation length parameter is taken to be $\beta_1 = \beta_2 = 1/5$ to ensure a realistic representation of the coarse-scale microstructure. A more detailed study of the correlation length parameter will be provided in Section 5.2. The Hurst parameters for generating the fine-scale fractional Brownian random field are $\mu = 0.8$ for the mild surface texture case, $\mu = 0.4$ for the medium surface texture case, and $\mu = 0.1$ for the strong surface texture case. The grid spacing of the rectangular 2D grid over $[0, \pi] \times [0, 2\pi]$ utilized in constructing the coarse-scale and fine-scale random fields is set to be $\Delta_1 = \Delta_2 = \pi/512$. Figure 17 shows the volume mesh for the smoothed aggregate microstructure, which is generated using 3D tetrahedral elements. It is shown that the proposed procedure has done a good job in generating concrete aggregate microstructure as well as the relevant mesh.

5.2. Effects of Critical Numerical Parameters on Particulate Microstructure Generation

As mentioned in Section 5.1, a number of numerical parameters are present in the modeling of aggregate microstructures, which may affect the simulated aggregate microstructures in different ways. In this subsection, the effects of critical numerical parameters on the simulated aggregate microstructures are discussed.

In simulating the coarse-scale microstructure, one of the critical parameters is the correlation length parameter in the covariance function of the stationary Gaussian random field, i.e., β_1 and β_2 in Equation 1. Figure 18 shows the simulated stationary Gaussian random fields for different correlation length parameters β_1 and β_2 . In

particular, Figure 18a has the highest correlation length parameter ($\beta_1 = \beta_2 = 1/5$), whereas Figure 18c has the lowest correlation length parameter ($\beta_1 = \beta_2 = 1/50$). It is shown that the correlation length parameters have a substantial impact on the frequency contents of the generated random fields. We can see that as the correlation length parameter gets lower, the topographic variation of the surface becomes more significant. In contrast to the coarse-scale microstructure, the fine-scale microstructure is influenced by the Hurst parameter, i.e., μ in Equation 9. Figure 19 plots the generated fractional Brownian random fields for different Hurst parameters. It is observed that the surface roughness of the generated fractional Brownian random field is highly affected by the Hurst parameter. Specifically, the fractional Brownian surface appears to be rougher when the Hurst parameter is smaller. It also follows from Figure 19 that the varying Hurst parameter allows for the representation of a wide range of surface textures ranging from the very simple to the very complex. This capability is in part attributed to the particular nature of the covariance function of the fractional Brownian random field, i.e., the undefined first derivative of the nonstationary covariance in Equation 9. In contrast, as the first and second derivatives of the covariance of function of the stationary Gaussian random field are well defined, the simulated random field seems to have a smoother surface pattern. Thus, the stationary Gaussian random field is better suited to representing the fundamental shape of a particulate microstructure, while the fractional Brownian random field has a better performance in simulating the surface texture of the microstructure.

In constructing the coarse-scale and the fine-scale microstructures, another important consideration is the number of data points that are utilized to sample the coarse-scale and the fine-scale random fields. For instance, if we sample the random field on a uniformly spaced grid on $[0, \pi] \times [0, 2\pi]$ with the number of sampled points $n_1 = 19$ and $n_2 = 37$, the grid spacings Δ_1 and Δ_2 become identically $\pi/18$ in both directions. Figure 20 depicts the generated microstructures for the example shown in Section 5.1 (Figure 16) using different grid spacings. It is clearly shown that to ensure a realistic simulation of aggregate microstructure, a sufficiently small grid size should be used. On the basis of the numerical results obtained from the present study, it is recommended that a grid size of $\Delta_1 = \Delta_2 \leq \pi/512$ should be considered in the simulation of the coarse-scale and fine-scale random fields in order to capture the complex morphological shape and surface texture effects.

5.3. Mesh Refinement Analysis for Particulate Microstructures

As mentioned in Section 4.2, the generation of the finite element mesh for the particulate microstructure may need some degree of refinement, especially in the regions of complex geometric shape. In this subsection, we examine

1
2
3 the performance of the proposed approach for handling local mesh refinement. In concert with the discussions in
4
5 Section 4.2, we proposed to use a multi-criterion-based shape quality metric that incorporates the curvature and
6
7 element aspect ratio of the mesh. The value of the metric may vary between 0 and 1. A higher value indicates a
8
9 better shape quality of the element. On the other hand, a value close to zero represents a poor element shape. In
10
11 order to identify the elements that need further refinement, we first compute the curvature of the mesh. Figure 21
12
13 shows the different surface meshes and the corresponding curvature plots of the aggregate microstructure presented
14
15 in Section 5.1. It is shown that the high curvature areas in the coarse mesh are mostly distributed around the
16
17 regions with sharp features, which is indicated by the magenta color shown in Figure 21a2. Upon refining the
18
19 coarse mesh, we obtain the medium mesh, which is shown in Figure 21b1. As shown in Figure 21b2, after mesh
20
21 refinement, the high curvature areas in the medium mesh are significantly reduced. When the surface mesh is further
22
23 refined (Figure 21c1), the morphological and topographical details of the microstructure appear to be clearer. The
24
25 variation of the curvature of the surface mesh is also observed to be smoother (Figure 21c2). Similar variation
26
27 patterns are also observed in the volume mesh plots shown in Figure 22. In Figure 22, Subplots a1, b1, and c1
28
29 exhibit the volumetric meshes of the aggregate microstructure presented in Section 5.1. It is noted that in Figure
30
31 22, the elements with poor quality are highlighted in red on the mesh Subplots a1, b1, and c1. It follows from Figure
32
33 22 that the elements with poor quality mostly occur in the region involving change of curvature, indicating that
34
35 additional mesh refinement may be needed in these local regions. It is also seen that the element shape becomes
36
37 increasingly better as the mesh is further refined. This is also reflected in the element quality histogram Subplots
38
39 a2, b2, and c2 of Figure 22. It is shown that as the mesh gets finer, the element shape quality gets better.
40
41

42
43 Depending on the type of problem encountered, the selection of the mesh refinement method is based on the
44
45 nature of the particular problem. Special care should be taken when meshing problems involving time-varying
46
47 loadings. For instance, time-adaptive mesh refinement methods are typically utilized to handle models involving
48
49 material nonlinearities and arbitrary time-varying excitations. In these methods, the remeshing process is solution-
50
51 dependent and performed at discrete time instances, which is based on the error estimate of the solution at each
52
53 time instance. In contrast, wavelength-adaptive mesh refinement methods are favored for linear models with applied
54
55 loadings consisting of a single frequency or a range of known frequencies. In this linear case, it is important that
56
57 the element size should be chosen sufficiently lower than the wavelength in order to make sure that the polynomial
58
59 basis functions used for the element resolve the waves.
60
61
62
63
64
65

1
2
3 Another point worth noting is that the aforementioned refinement techniques will converge towards the solution
4
5 at different rate. Under certain circumstances, some mesh refinement strategy may converge much faster than others.
6
7 To achieve optimal convergence rates, a different strategy would be to exploit the unfitted or non-conforming finite
8
9 element method. In this method, the description of the geometry is decoupled from the representation of the solution.
10
11 As a result, the boundary of the computational domain is represented on a background grid, which significantly
12
13 alleviates the meshing burden in the standard finite element method. In the context of the unfitted finite element
14
15 method, a notable approach is the Cut Finite Element Method (CutFEM) [64–68], which enriches the solution space
16
17 by overlaying cut elements. For instance, Susanne and Kerfriden developed CutFEM algorithms for the modeling
18
19 of two-phase flow problems [66] as well as the simulation of multiple unilateral contact problems [67]. Following the
20
21 methodology presented in [66, 67], Kerfriden, Susanne, and Mihai [68] also proposed a mix-dimensional CutFEM
22
23 solver for fiber-reinforced composites. It would be interesting to combine the CutFEM method and the present
24
25 approach, which will be addressed in a future study.
26
27
28

29 *5.4. Generation of Mesostructural RVEs of Cementitious Composites*

30
31

32 Following the examples presented in the previous subsections, this subsection illustrates and verifies the ca-
33
34 pability of the proposed approach for the morphology and mesh generation of mesoscopic RVEs of cementitious
35
36 composites, which are shown in Figures 23-30. It is noted that the numerical parameters utilized in this subsection
37
38 are identical to those presented in Section 5.1. Four different scenarios are considered in this illustration problem,
39
40 i.e., Scenario 1 (Figures 23-24), Scenario 2 (Figures 25-26), Scenario 3 (Figures 27-28), Scenario 4 (Figures 29-30).
41
42 These four scenarios can be further classified into two groups, i.e., Group 1 (Figures 23-26) and Group 2 (Figures
43
44 27-30). Specifically, the shape of Group 1 is more rounded and regular. On the other hand, in Group 2, the
45
46 microstructural inclusions look sharper and more irregular. It is also noted that for both groups, RVEs with both
47
48 low and high packing densities are provided. Meanwhile, for each group, four different cases of surface texture are
49
50 generated, i.e., no surface texture, mild surface texture, medium surface texture, and strong surface texture. The
51
52 RVE microstructures for the four scenarios are shown in Figures 23, 25, 27, and 29. The corresponding volume
53
54 meshes for the four scenarios are displayed in Figures 24, 26, 28, and 30. It is shown that the proposed method
55
56 is capable of realistically simulating the complex geometric shape and surface texture of cementitious composite
57
58 microstructures as well as generating high-quality finite element meshes of cementitious composite microstructures.
59
60
61
62
63
64
65

5.5. Comparison of the Proposed Procedure to Existing Experimental Results and Computational Models

To validate and exemplify the proposed procedure, in this subsection, we compare the particulate microstructures generated by the proposed procedure and those obtained from experimental and numerical studies reported in the literature. To this aim, we first compare the aggregates generated using the present approach to real concrete aggregates. In generating the virtual aggregate microstructural samples, the numerical parameters utilized in Section 5.1 are adopted. Figures 31 and 33 present a number of selected natural gravels and crushed rocks of different shapes and sizes, which are the two main types of concrete aggregates used in construction and building materials. Figures 32 and 34 present the two types of aggregates generated using the present procedure. It is shown that the present procedure is capable of simulating the morphological shape for aggregates of natural gravels and crushed rocks.

To better illustrate the surface texture effects of aggregate microstructures, Figure 35 presents the image of a selected aggregate with a rough surface texture and the magnified view of the surface texture. It follows from Figure 35 that if we zoom in and take a closer look at the magnified view of the aggregate microstructure, the more sophisticated surface texture emerges. Similar surface texture effects are also observed in the laser scanned 3D aggregate microstructure shown in Figure 36. As shown earlier in Figures 4 and 16, such intricate surface details can be well captured by the present procedure. To further illustrate the capability of the present approach, in addition to the two cases shown in Figures 4 and 16, an additional case with more complex surface texture is provided in Figure 37. It follows from the aforementioned generated microstructural samples that the present methodology is capable of representing the very fine details of surface texture across different length scales in a realistic manner, which yields distinct advantages over conventional morphology generation methods and algorithms. Since surface roughness may exert substantial impact on the mechanical properties of the inclusion-matrix interface, it should be considered in the simulation procedure. It is however noted that due to the complexities involved, such surface texture effects are normally neglected in most of the existing simulation approaches, which will be discussed shortly in this subsection.

Following the comparison of the real and virtual particle shapes, we further verify the performance of the present procedure to generate RVE microstructures by comparing the computationally generated and the experimentally determined cement-based RVE microstructures. To this aim, Figures 38b1 and 38b2 show the 2D cross sections of computationally generated 3D cementitious composite RVEs with different types of aggregates. For comparison

1
2
3 purposes, typical 2D cross sections obtained from experimental RVE samples are shown in Figures 38a1 and 38a2. It
4
5 follows from Figure 38 that the proposed procedure is capable of simulating the RVE microstructures of cementitious
6
7 composites in a fairly realistic fashion.

8
9 In addition to the aforementioned comparison, we also compare our proposed approach to contemporary compu-
10
11 tational models for generating granular geo-microstructures. Table 1 summarizes the important articles regarding
12
13 the advanced modeling approaches developed for simulating granular geo-microstructures. As shown in Table 1, a
14
15 commonly utilized approach for the simulation of geo-microstructures is the approach using spherical harmonics.
16
17 Figures 39a-c show the microstructure regenerated from the aggregate example shown in Figure 37 using the spher-
18
19 ical harmonic representation scheme. Upon comparing Figures 39a-c to Figures 39e-f, we first notice that the shape
20
21 of the aggregate microstructure looks more realistic as the number of terms used in the spherical harmonic series
22
23 expansion is increased. However, we can also see that although the spherical harmonic approach generally does a
24
25 good job in representing the overall shape of the microstructure, it is not capable of representing the complex surface
26
27 roughness and topographical details for any desired level of satisfaction. In addition, one of the major limitations of
28
29 the conventional spherical harmonics is the property of the spherical harmonic series near discontinuities, i.e., the
30
31 Gibbs Phenomenon (e.g., [52–54]). In general, spherical harmonics can be used to approximate smooth geometric
32
33 shapes reasonably well. However, for complex geometries with distinct local features and strong discontinuities
34
35 such as the surface texture of a particulate microstructure considered in the present study, even a large number of
36
37 spherical harmonics may not be sufficient to represent the surface topographic details. An alternative is to rely on
38
39 surface reconstruction of 3D microstructural point clouds (e.g., [23]). Figure 39d shows the reproduced 3D aggregate
40
41 microstructure using the alpha shape approach in [23]. It is clearly seen that the microstructure generated using
42
43 the alpha shape approach shows a poor performance in capturing the fundamental shape and surface detail of the
44
45 aggregate. Thus, the alpha shape approach is probably a better fit for representing crushed-rock-type aggregate
46
47 microstructures that possess sharp and irregular geometric characteristics. It is also worth mentioning that in
48
49 these aforementioned contemporary research works, focus is placed on the generation of the morphological shape of
50
51 granular geo-microstructures. The mesh generation of these granular geo-microstructures has not been discussed.
52
53
54
55
56
57
58
59
60
61
62
63
64
65

6. Closure

6.1. Concluding Remarks

In this work, a computational framework and methodology is proposed for the morphology simulation and mesh generation of particulate composite microstructures. After that, a hybrid computational-experimental approach is introduced for the shape optimization of the generated microstructure. In addition, the solution technique for local mesh refinement is also presented. The developed numerical approach is implemented and applied to generate microstructures of particulate composite materials as well as the corresponding surface and volume meshes. A number of illustration and verification examples are presented to showcase the proposed method. It is shown that the proposed methodology is capable of simulating high-quality particulate composite microstructures. The proposed method also demonstrates its performance in parameterizing and smoothing surface meshes and generating volume meshes, opening up new ways for probing into many complex micromechanical phenomena and mechanisms of particulate composite materials.

At this point, it should be noted that the focus of the present study is to present a computational framework for morphology simulation and mesh generation of high-quality particulate composite microstructures with complex surface texture, in the hope of reducing the difficulties associated with meshing complex geometries. Clearly, there are alternative options for handling complex geometries. One of such methods is the implicit representation scheme that relies on the Level Set Method [69] to describe the geometric features of domain interfaces and boundaries. Instead of utilizing a conforming mesh to represent complex geometries, the implicit representation scheme defines the geometrical features on a fixed background mesh, thus simplifying the mesh generation process. Along this line, Moumnassi et al. [70, 71] developed parametric and implicit level set representation of arbitrary objects with complex geometrical features. It is however noted that only the coarse-scale geometric surface is considered in their studies. The robust and accurate implicit representation of the fine-scale particulate microstructural surface still poses a challenge. To capture the extremely intricate surface texture of the fine-scale surface, the Gradient-enhanced Level Set Method (GeLSM) (e.g., [72]) may be the way to go. The coupling of the present morphology simulation approach and the Gradient-enhanced Level Set implicit representation scheme will be presented in a future communication.

6.2. Recommendations for Future Research

Following the morphology and mesh generation of particulate composite microstructures, the next step is to apply the proposed algorithm to investigate the multiscale behaviors of particulate composite materials. To achieve this goal, special attention should be paid to the simulation of problems involving discontinuities such as interface and fracture. When it comes to solving partial differential equations with discontinuous solutions, there is a suite of numerical approaches that have been developed in the literature. Within the framework of the finite element method, two typical numerical methods could be used to represent cracks and fractures: the methods based on continuum damage mechanics (e.g., [73–75]) and the phase field method (e.g., [76–78]). The continuum damage mechanics-based approaches provide a general capability for modeling inelastic mechanical behaviors of particulate composite materials. For instance, Nguyen et al. [75] conducted 3D mesoscopic analysis of foamed concrete using the damage plasticity model and X-ray Computed Tomography. However, the major drawback of this type of approach is that it suffers from the problem of mesh dependency of the results. The issue of mesh sensitivity can be remedied through the use of numerical techniques such as viscoplastic regularization schemes or nonlocal damage models. Alternatively, an emerging family of methods for modeling cracks and fractures is the phase field method. The phase field method belongs to the category of diffusive interface methods. However, since the phase field method is based on using a smoothing region to represent the interface, a comparatively large number of elements are required to capture the interface region. On the other hand, one may employ sharp interface methods (e.g., the XFEM [79–81] and the CutFEM [64–68]) to represent cracks and fractures, in which less elements are needed to represent the interface region. In particular, by coupling the FEM and the Partition of Unity Method (PUM), the XFEM incorporates discontinuities and singularities into the solution space by using special enrichment functions along with additional degrees of freedom. For instance, Menk and Bordas [82] presented a XFEM methodology to model crack propagation in solder joints considering microstructural phenomena. To represent multiple discontinuities present in an enriched element, Bansal et al. [83] developed a multi-split XFEM approach for the analysis of heterogeneous materials including pores and reinforcement particles. As an extension of the conventional XFEM, the Smoothed Extended Finite Element Method (SmXFEM) [84–87] combined the notion of strain smoothing with the XFEM to account for the effects of interfaces. On the other hand, the CutFEM [64–68] enriches the solution through the introduction of overlapping fictitious domains. In both methods, as the computation is performed on a fixed background mesh, the finite element mesh does not need to conform to the geometry of the crack and inclusion

1
2
3 boundary, thus significantly reducing the difficulties in mesh generation and refinement. The research on coupling
4
5 the present algorithm with the PFM and the XFEM is currently underway and, hopefully, will be presented in
6
7 subsequent studies.

8
9 Future research can also be directed towards microstructure optimization and material design of particulate
10
11 composite materials. Generally, two main types of numerical schemes have been developed in the literature to
12
13 solve optimization problems, i.e., deterministic optimization algorithms and stochastic optimization algorithms.
14
15 Depending on whether the objective function is differentiable or not, the optimization algorithms using deterministic
16
17 methods can be further divided into two groups: algorithms relying on derivative information and algorithms
18
19 without considering derivative information. On the other hand, due to the exploitation of randomness in the search
20
21 procedure, stochastic optimization algorithms increase the probability of the procedure finding the global optima of
22
23 the objective function. The commonly utilized approaches in this category include the Genetic Algorithm and the
24
25 Particle Swarm Optimization Algorithm. For instance, the Operator-Split Genetic Algorithm proposed in [24] can be
26
27 employed to optimize the particulate microstructure generated by the present procedure. Additionally, optimization
28
29 algorithms also provide an effective means of designing and optimizing materials. For instance, Hoang [88] proposed
30
31 a concurrent topology optimization method for porous materials using the principle of linear superposition and the
32
33 projection technique of adaptive geometric components. Generally, the major division in topology optimization for
34
35 porous material design is how the loading is treated in the model. Through the combination of moving morphable
36
37 bars and the consideration of loading uncertainties, the proposed algorithm is capable of simultaneously optimizing
38
39 both the macroscale and microscale structures by minimizing the weighted sum of the expected compliance and
40
41 standard deviation. It would be interesting to integrate the optimization algorithm and the present method for
42
43 the design and optimization of cementitious materials, which will be presented in a future research work. In order
44
45 to achieve an improved optimization performance, the optimization procedure presented in Section 4 could also be
46
47 paired with machine learning algorithms. More specifically, the image processing procedure, the multi-cut method,
48
49 and the real aggregate database presented in Section 4 can be used to train the machine learning model. Once the
50
51 model is trained, it can be used to tell whether the simulated particle morphology is good or not. In addition, the
52
53 machine learning algorithms developed in [89, 90] can also be utilized to predict the strength, damage, and fracture
54
55 behaviors of particle composite materials.
56
57

58
59 An additional point worth mentioning is that the material behaviors and mechanical properties at higher scales
60
61
62
63
64
65

1
2
3 are closely related to the microstructure geometries at lower scales. For instance, at the nanometer scale, cement-
4
5 based particle composite materials such as concrete are composed of Calcium-Silicate-Hydrate (C-S-H) gels, which
6
7 is the main product of cement hydration. At the micrometer scale, concrete is characterized by the cement paste
8
9 consisting of individual cement grains. At the mesoscale, concrete can be viewed as a three-phase composite of
10
11 the cement paste, the aggregates, and the Interfacial Transition Zone (ITZ). As a result of the multiscale internal
12
13 structure of concrete, the pore structure of concrete at the mesoscopic and microscopic levels is strongly influenced by
14
15 the hydration process that takes place at the nanoscale level. A thorough and systematic investigation of these cross-
16
17 scale behaviors could be realized by using multiscale methods that couples nanoscale models to continuum models.
18
19 Computational homogenization is then used to bridge the gap between the multiscale models. In general, such
20
21 models can be classified into three groups, i.e., hierarchical models, semiconcurrent models, and concurrent models.
22
23 The interested reader is referred to [91, 92] for a detailed description of these methods. It is also noted that because
24
25 different numerical methods are developed in different software frameworks, the implementation of multiscale models
26
27 may also require the coupling of different software packages, which poses an additional challenge. A number of
28
29 open-source software frameworks have been reported in the literature. In these open-source software frameworks,
30
31 computing platforms developed based on continuum-based methods include, but not limited to FEAPPV [93],
32
33 FEniCS [94, 95], and KRATOS [96–98]. For the software packages using discrete methods, YADE [99], LAMMPS
34
35 [100], and PERMIX [92] could be used. A review of these open-source software frameworks can be found in [91, 92].
36
37
38

- 39
40 [1] W. Xu, H. Chen, Z. Lv, A 2D elliptical model of random packing for aggregates in concrete, *J. Wuhan Univ.*
41
42 *Technol. - Materials Science Edition* 25 (2010) 717-720.
43
44 [2] P. Fu, Y.F. Dafalias, Fabric evolution within shear bands of granular materials and its relation to critical state
45
46 theory, *Int. J. Numer. Anal. Methods Geomech.* 35 (2011) 1918-1948.
47
48 [3] Z.M. Wang, A.K.H. Kwan, H.C. Chan, Mesoscopic study of concrete I: generation of random aggregate struc-
49
50 ture and finite element mesh, *Comput. Struct.* 70 (1999) 533-544.
51
52 [4] A.K.H. Kwan, Z.M. Wang, H.C. Chan, Mesoscopic study of concrete II: nonlinear finite element analysis,
53
54 *Comput. Struct.* 70 (1999) 545-556.
55
56 [5] C.B. Du, L.G. Sun. Numerical simulation of aggregate shapes of two-dimensional concrete and its application,
57
58 *J. Aerosp. Eng.* 20 (2007) 172-178.
59
60 [6] S.M. Kim, R.K. Abu Al-Rub, Meso-scale computational modeling of the plastic-damage response of cementi-
61
62
63
64
65

- 1
2
3 tious composites, *Cem. Concr. Res.* 41 (2011) 339-358.
4
5 [7] P. Wriggers, S.O. Moftah, Mesoscale models for concrete: Homogenisation and damage behavior, *Finite Elem.*
6
7 *Anal. Des.* 42 (2006) 623-636.
8
9 [8] K. Sobolev, A. Amirjanov, Application of genetic algorithm for modeling of dense packing of concrete aggre-
10
11 gates, *Constr. Build. Mater.* 24 (2010) 1449-1455.
12
13 [9] J.P.B. Leitea , V. Slowikb, H. Mihashi, Computer simulation of fracture processes of concrete using mesolevel
14
15 models of lattice structures, *Cem. Concr. Res.* 34 (2004) 1025-1033.
16
17 [10] W. Xu, H. Chen, Microstructural modelling of cement-based materials via random packing of three-dimensional
18
19 ellipsoidal particles, *Procedia Eng.* 27 (2012) 332-340.
20
21 [11] T.T. Ng, Particle shape effect on macro- and micro-behavior of monodisperse ellipsoids, *Int. J. Numer. Anal.*
22
23 *Methods Geomech.* 33 (2009) 511-527.
24
25 [12] X. Lin, T.T. Ng. A three-dimensional discrete element model using arrays of ellipsoids, *Geotechnique* 47 (1997)
26
27 319-329.
28
29 [13] A.A. Pena, R. Garcia-Rojo, H.J. Herrmann, Influence of particle shape on sheared dense granular media,
30
31 *Granul. Matter* 9 (2007) 279-291.
32
33 [14] S. Hafner, S. Eckardt, T. Luther, C. Konke, Mesoscale modeling of concrete: Geometry and numerics, *Comput.*
34
35 *Struct.* 84 (2006) 450-461.
36
37 [15] G. Mollon, J. Zhao, Fourier-Voronoi-based generation of realistic samples for discrete modelling of granular
38
39 materials, *Granul. Matter* 14 (2012) 621-638.
40
41 [16] G. Mollon, J. Zhao, 3D generation of realistic granular samples based on random fields theory and Fourier
42
43 shape descriptors, *Comput. Methods Appl. Mech. Engrg.* 279 (2014) 46-65.
44
45 [17] M. Grigoriu, E.J. Garboczi, C. Kafali, Spherical harmonic-based random fields for aggregates used in concrete,
46
47 *Powder Technol.* 166 (2006) 123-138.
48
49 [18] E.J. Garboczi, Three-dimensional mathematical analysis of particle shape using X-ray tomography and spher-
50
51 ical harmonics: application to aggregates used in concrete, *Cem. Concr. Res.* 32 (2002) 1621-1638.
52
53 [19] B. Zhou, J. Wang, Random generation of natural sand assembly using micro X-ray tomography and spherical
54
55 harmonics, *Geotech. Lett.* 1 (2015) 6-11.
56
57 [20] B. Zhou, J. Wang, Generation of a realistic 3D sand assembly using X-ray micro-computed tomography and
58
59
60
61
62
63
64
65

- 1
2
3 spherical harmonic-based principal component analysis, *Int. J. Numer. Anal. Methods Geomech.* 41 (2017)
4
5 93-109.
6
7 [21] D. Wei, J. Wang, J. Nie, B. Zhou, Generation of realistic sand particles with fractal nature using an improved
8
9 spherical harmonic analysis, *Comput. Geotech.* 104 (2018) 1-12.
10
11 [22] J. Huang, Q. Peng, A fast algorithm for multifield representation and multiscale simulation of high-quality 3D
12
13 stochastic aggregate microstructures by concurrent coupling of stationary Gaussian and fractional Brownian
14
15 random fields, *Internat. J. Numer. Methods Engrg.* 115 (2018) 328-357.
16
17 [23] J. Huang, Q. Peng, X. Hu, Y. Du, A combined-alpha-shape-implicit-surface approach to generate 3D random
18
19 concrete mesostructures via digital image processing, spectral representation, and point cloud, *Constr. Build.*
20
21 *Mater.* 143 (2017) 330-365.
22
23 [24] J. Huang, Generation of realistic 3D concrete aggregate microstructures using multiscale multifractal evolu-
24
25 tionary stochastic manifold and operator-split-genetic algorithm, *Probabilistic Eng. Mech.* 66 (2021) 103164.
26
27 [25] A.X. Jerves, R.Y. Kawamoto, J.E. Andrade, Effects of grain morphology on critical state: a computational
28
29 analysis, *Acta Geotech.* 11 (2016) 493-503.
30
31 [26] R. Kawamoto, E. Andrade, G. Viggiani, J.E. Andrade, Level set discrete element method for three-dimensional
32
33 computations with triaxial case study, *J. Mech. Phys. Solids* 91 (2016) 1-13.
34
35 [27] S. Naderi, M. Zhang, An integrated framework for modelling virtual 3D irregulate particulate mesostructure,
36
37 *Powder Technol.* 355 (2019) 808-819.
38
39 [28] S. Naderi, M. Zhang, A novel framework for modelling the 3D mesostructure of steel fibre reinforced concrete,
40
41 *Comput. Struct.* 234 (2020) 106251.
42
43 [29] S. Naderi, W. Tu, M. Zhang, Meso-scale modelling of compressive fracture in concrete with irregularly shaped
44
45 aggregates, *Cem. Concr. Res.* 140 (2021) 106317.
46
47 [30] S. Naderi, M. Zhang, Meso-scale modelling of static and dynamic tensile fracture of concrete accounting for
48
49 real-shape aggregates, *Cem. Concr. Compos.* 116 (2021) 103889.
50
51 [31] Y. Ito, K. Nakahashi, Direct surface triangulation using stereolithography data, *AIAA J.* 40 (3) (2002) 490-496.
52
53 [32] E. Bechet, J.C. Cuilliere, F. Trochu, Generation of a finite element mesh from stereolithography (stl) files,
54
55 *Comput. Aided Des.* 34 (1) (2002) 1-17.
56
57 [33] H. Borouchaki, P. Laug, P. George, Parametric surface meshing using a combined advancing-front generalized
58
59
60
61
62
63
64
65

- 1
2
3 delaunay approach, *Internat. J. Numer. Methods Engrg.* 49 (2000) 223-259.
4
5 [34] Y. Zheng, N. Weatherill, O. Hassan, Topology abstraction of surface models for three-dimensional grid gener-
6 ation, *Eng. Comput.* 17 (2001) 28-38.
7
8
9 [35] D.L. Marcum, Efficient generation of high-quality unstructured surface and volume grids, *Eng. Comput.* 17 (3)
10 (2001) 211-233.
11
12
13 [36] P. Laug, H. Boruchaki, Interpolating and meshing 3d surface grids, *Internat. J. Numer. Methods Engrg.* 58
14 (2003) 209-225.
15
16
17 [37] M. Attene, B. Falcidieno, M. Spagnuolo, G. Wyvill, A mapping-independent primitive for the triangulation of
18 parametric surfaces, *Graph. Models* 65 (2003) 260-273.
19
20
21 [38] M.S. Floater, Parametrization and smooth approximation of surface triangulations, *Comput. aided Geom. Des.*
22 14 (1997) 231-250.
23
24
25 [39] M.S. Floater, K. Hormann, Surface parameterization: a tutorial and survey, *Advances in Multiresolution for*
26 *Geometric Modelling* (2005) 157-186.
27
28
29 [40] J.F. Remacle, C. Geuzaine, G. Compere, E. Marchandise, High quality surface remeshing using harmonic maps,
30 *Internat. J. Numer. Methods Engrg.* 83 (2010) 403-425.
31
32
33 [41] D.F. Watson, Computing the n-dimensional Delaunay tessellation with application to Voronoi polytopes, *Com-*
34 *put J.* 24 (2) (1981) 167-172.
35
36
37 [42] R. Lohner, P. Parikh, Generation of three-dimensional unstructured grids by the advancing-front method,
38 *Internat. J. Numer. Methods Fluids* 8 (10) (1988) 1135-1149.
39
40
41 [43] T.D. Blacker, R.J. Meyers, Seams and wedges in plastering: A 3-D hexahedral mesh generation algorithm,
42 *Eng. Comput.* 9 (2) (1993) 83-93.
43
44
45 [44] T.J. Tautges, T. Blacker, S.A. Mitchell, The whisker weaving algorithm: A connectivity-based method for
46 constructing all-hexahedral finite element meshes, *Internat. J. Numer. Methods Engrg.* 39 (19) (1996) 3327-
47 3349.
48
49
50 [45] M.L. Staten, S.A. Canann, S.J. Owen, BMSweep: Locating interior nodes during sweeping, *Eng. Comput.* 15
51 (3) (1999) 212-218.
52
53
54 [46] M.A. Yerry, M.S. Shephard, Automatic three-dimensional mesh generation by the modified-octree technique,
55 *Internat. J. Numer. Methods Engrg.* 20 (11) (1984) 1965-1990.
56
57
58
59
60
61
62
63
64
65

- 1
2
3 [47] C.R. Dietrich, G.N. Newsam, Fast and exact simulation of stationary Gaussian processes through circulant
4 embedding of the covariance matrix, *SIAM J. Sci. Comput.* 18 (1997) 1088-1107.
5
6
7 [48] G.J. Lord, C.E. Powell, T. Shardlow, *An introduction to computational stochastic PDEs*, Cambridge University
8 Press, New York, 2014.
9
10 [49] B. Mandelbrot, J.W. van Ness, Fractional brownian motions, fractional noises and applications, *SIAM Rev.* 10
11 (1968) 422-437.
12
13 [50] D.P. Kroese, I.B. Zdravko IB, *Spatial Process Simulation*, in *Stochastic Geometry, Spatial Statistics and*
14 *Random Fields: Models and Algorithms*. Cham, Switzerland: Springer; 2015.
15
16 [51] P.T. Choi, K.C. Lam, L.M. Lui, FLASH: Fast landmark aligned spherical harmonic parameterization for
17 genus-0 closed brain surfaces, *SIAM J. Imaging Sci.* 8 (2015) 67-94.
18
19 [52] M.K. Chung , L. Shen , K.M. Dalton , R.J. Davidson, Multi-scale voxel-based morphometry via weighted
20 spherical harmonic representation, *Proceedings of the Third International Workshop on Medical Imaging and*
21 *Virtual Reality.* (2006) 36-43.
22
23 [53] M.K. Chung, R. Hartley, K.M. Dalton, R.J. Davidson, Encoding cortical surface by spherical harmonics, *Stat.*
24 *Sinica* 18 (2008) 1269-1291.
25
26 [54] M.K. Chung, Kim M. Dalton, and Richard J. Davidson, Tensor-based cortical surface morphometry via
27 weighted spherical harmonic representation, *IEEE Trans. Med. Imaging* 27 (8) (2008) 1143-1151.
28
29 [55] M. Pauly, M. Gross, L.P. Kobbelt, Efficient simplification of point-sampled surfaces, *Proceedings of IEEE*
30 *Visualization.* (2002) 163-170.
31
32 [56] R.C. Gonzalez, R.E. Woods, S.L. Eddins, *Digital Image Processing Using MATLAB*, New Jersey, Pearson
33 Prentice Hall, 2004.
34
35 [57] L. Demkowicz, Ph. Devloo, J.T. Oden, On an h-type mesh-refinement strategy based on minimization of
36 interpolation errors, *Comput. Methods Appl. Mech. Eng.* 53(1) (1985) 67-89.
37
38 [58] T. Belytschko, M. Tabbara, H-adaptive finite element methods for dynamic problems, with emphasis on local-
39 ization, *Int. J. Numer. Methods Eng.* 36(24) (1993) 4245-4265.
40
41 [59] P. Diez, A. Huerta, A unified approach to remeshing strategies for finite element h-adaptivity, *Comput. Methods*
42 *Appl. Mech. Eng.* 176(1) (1999) 215-229.
43
44 [60] A. Brandt, Rigorous quantitative analysis of multigrid I: constant coefficients two-level cycle with L_2 -norm,
45
46
47
48
49
50
51
52
53
54
55
56
57
58
59
60
61
62
63
64
65

- 1
2
3 SIAM J. Numer. Anal. 31(6) (1994) 1695-1730.
4
5 [61] D. Bai, A. Brandt, Local mesh refinement multilevel techniques, SIAM J. Sci. Stat. Comput. 8(2) (1987)
6
7 109-134.
8
9 [62] M.J. Berger, J. Olinger, Adaptive mesh refinement for hyperbolic partial differential equations, J. Comput.
10
11 Phys. 53(3) (1984) 484-512.
12
13 [63] L.A. Shirman, Construction of smooth curves and surfaces from polyhedral models (Ph.D. dissertation). Uni-
14
15 versity of California at Berkeley, Berkeley, California, 1990.
16
17 [64] A. Hansbo, P. Hansbo, An unfitted finite element method based on Nitsche's method for elliptic interface
18
19 problems, Comput. Methods Appl. Mech. Eng. 191 (2002) 5537-5552.
20
21 [65] E. Burman, S. Claus, P. Hansbo, M.G. Larson, A. Massing, CutFEM: Discretizing geometry and partial
22
23 differential equations, Int. J. Numer. Methods Eng. 104(7) (2014) 472-501.
24
25 [66] S. Claus, P. Kerfriden, A CutFEM method for two-phase flow problems, Comput. Methods Appl. Mech. Eng.
26
27 348 (2019) 185-206.
28
29 [67] S. Claus, P. Kerfriden, A stable and optimally convergent LaTIn-CutFEM algorithm for multiple unilateral
30
31 contact problems, Int. J. Numer. Methods Eng. 113(6) (2018) 938-966.
32
33 [68] P. Kerfriden, S. Claus, I. Mihai, A mixed-dimensional CutFEM methodology for the simulation of fibre-
34
35 reinforced composites, Adv. Model. and Simul. in Eng. Sci. 7 (2020) 18.
36
37 [69] S. Osher, J.A. Sethian, Fronts propagating with curvature-dependent speed: algorithms based on hamilton-
38
39 Jacobi formulations, J. Comput. Phys. 79 (1988) 2-49.
40
41 [70] M. Moumnassi, S. Belouettar, E. Bechet, S.P.A. Bordas, D. Quoirin, M. Potier-Ferry. Finite element analysis
42
43 on implicitly defined domains: An accurate representation based on arbitrary parametric surfaces, Comput.
44
45 Methods Appl. Mech. Engrg. 200 (2011) 774-796.
46
47 [71] M. Moumnassi, S.P.A. Bordas, R. Figueredo, P. Sansen, Analysis using higher-order XFEM: implicit represen-
48
49 tation of geometrical features from a given parametric representation, Mech. Ind. 15 (2014) 443-448.
50
51 [72] J.-C. Nave, R.R. Rosales, B. Seibold, A gradient-augmented level set method with an optimally local, coherent
52
53 advection scheme, J. Comput. Phys. 229 (2010) 3802-3827.
54
55 [73] J. Lee, G. L. Fenves. Plastic-damage model for cyclic loading of concrete structures, J. Eng. Mech. 124 (1998)
56
57 892-900.
58
59
60
61
62
63
64
65

- 1
2
3 [74] J. Lubliner, J. Oliver, S. Oller, et al. A plastic-damage model for concrete, *Int. J. Solids Struct.* 25 (1989)
4 229-326.
5
6
7 [75] T. Nguyen, A. Ghazlan, A. Kashani, S. Bordas, T. Ngo. 3D meso-scale modelling of foamed concrete based on
8 X-ray Computed Tomography, *Constr. Build. Mater.* 188 (2018) 583-598
9
10
11 [76] G.A. Francfort, J.J. Marigo, Revisiting brittle fracture as an energy minimization problem, *J. Mech. Phys.*
12 *Solids* 46 (1998) 1319-1342.
13
14
15 [77] C. Miehe, M. Hofacker, F. Welschinger, A phase field model for rate-independent crack propagation: robust
16 algorithmic implementation based on operator splits, *Comput. Methods Appl. Mech. Engrg.* 199 (2010) 2765-
17 2778.
18
19
20
21
22 [78] M.J. Borden, T.J.R. Hughes, C.M. Landis, C.V. Verhoosel, A higher-order phasefield model for brittle fracture:
23 Formulation and analysis within the isogeometric analysis framework, *Comput. Methods Appl. Mech. Engrg.*
24 273 (2014) 100-118.
25
26
27
28 [79] T. Belytschko, T. Black, Elastic crack growth in finite elements with minimal remeshing, *Internat. J. Numer.*
29 *Methods Engrg.* 45 (1999) 601-620.
30
31
32
33 [80] M. Stolarska, D.L. Chopp, N. Mos, T. Belytschko, Modelling crack growth by level sets in the extended finite
34 element method, *Internat. J. Numer. Methods Engrg.* 51 (2001) 943-960.
35
36
37 [81] S.P.A. Bordas, P.V. Nguyen, C. Dunant, A. Guidoum, N.-D. Hung, An extended finite element library, *Internat.*
38 *J. Numer. Methods Engrg.* 71 (2007) 703-732.
39
40
41 [82] A. Menk, S.P.A. Bordas, Crack growth calculations in solder joints based on microstructural phenomena with
42 X-FEM, *Comput. Mater. Sci.* 50 (2011) 1145-1156.
43
44
45 [83] M. Bansal, I.V. Singh, B.K. Mishra, S.P.A. Bordas, A parallel and efficient multi-split XFEM for 3-D analysis
46 of heterogeneous materials, *Comput. Methods Appl. Mech. Engrg.* 347 (2019) 365-401.
47
48
49 [84] S.P.A. Bordas, T. Rabczuk, N.-X. Hung, V.P. Nguyen, S. Natarajan, T. Bog, D.M. Quan, N.V. Hiep, Strain
50 smoothing in FEM and XFEM, *Comput. Struct.* 88 (2010) 1419-1443.
51
52
53 [85] X. Zhao, R. Duddu, S.P.A. Bordas, J. Qu, Effects of elastic strain energy and interfacial stress on the equilibrium
54 morphology of misfit particles in heterogeneous solids, *J. Mech. Phys. Solids.* 61 (2013) 1433-1445.
55
56
57 [86] X. Zhao, S.P.A. Bordas, J. Qu. A hybrid smoothed extended finite element/level set method for modeling
58 equilibrium shapes of nano-inhomogeneities, *Comput. Mech.* 52 (2013) 1417-1428.
59
60
61
62
63
64
65

- 1
2
3 [87] S. Natarajan, D.R. Mahapatra, S.P.A. Bordas. Integrating strong and weak discontinuities without integration
4 subcells and example applications in an XFEM/GFEM framework, *Int. J. Numer. Meth. Engng.* 83 (2010)
5 269-294.
6
7
8
9 [88] V.-N. Hoang, T. Pham, S. Tangaramvong, S.P.A. Bordas, H. Nguyen-Xuan. Robust adaptive topology opti-
10 mization of porous infills under loading uncertainties, *Struct. Multidiscipl. Optim.* 63 (2021) 2253-2266.
11
12
13 [89] T. Nguyen, A. Kashani, T. Ngo, S.P.A. Bordas, Deep neural network with high-order neuron for the prediction
14 of foamed concrete strength, *Comput-aided Civ. Inf.* 34(4) (2019) 316-332.
15
16
17 [90] C. Yang, Y. Kimb, S. Ryu, G.X. Gua. Prediction of composite microstructure stress-strain curves using con-
18 volutional neural networks, *Mater. Des.* 189 (2020) 108509.
19
20
21 [91] P.R. Budarapu, X. Zhuang, T. Rabczuk, S.P.A. Bordas, Chapter One - Multiscale modeling of material failure:
22 Theory and computational methods, *Adv. Appl. Mech.* 52 (2019) 1-103.
23
24
25 [92] H. Talebi, M. Silani, S.P.A. Bordas, P. Kerfriden, T. Rabczuk, A computational library for multiscale modeling
26 of material failure, *Comput. Mech.* 53 (2014) 1047-1071.
27
28
29 [93] FEAPpv: A Finite Element Analysis Program: Personal Version, companion to The Finite Element Method,
30 7th edition, Volumes 1 and 2 by O.C. Zienkiewicz and R.L. Taylor.
31
32
33 [94] M.S. Alnaes, J. Blechta, J. Hake, A. Johansson, B. Kehlet, A. Logg, C. Richardson, J. Ring, M.E. Rognes and
34 G.N. Wells. The FEniCS Project Version 1.5, *Archive of Numerical Software* 3, 2015.
35
36
37 [95] A. Logg, K.-A. Mardal, G. N. Wells et al. *Automated Solution of Differential Equations by the Finite Element*
38 *Method*, Springer, 2012.
39
40
41 [96] P. Dadvand, R. Rossi, E. Oate, An object-oriented environment for developing finite element codes for multi-
42 disciplinary applications, *Arch. Computat. Methods Eng.* 17 (2010) 253-297.
43
44
45 [97] P. Dadvand, R. Rossi, M. Gil, X. Martorell, J. Cotela, E. Juanpere, S. Idelsohn, E. Oate, Migration of a generic
46 multi-physics framework to HPC environments, *Comput. Fluids* 80 (2013) 301-309.
47
48
49 [98] V. Mataix Ferrandiz, P. Bucher, R. Rossi, J. Cotela, J.M. Carbonell, R. Zorrilla, R. Tosi, *KratosMultiphysics*
50 (Version 8.1). Zenodo, 2020.
51
52
53 [99] V. Smilauer et al., *Yade Documentation 3rd ed. The Yade Project*, 2021.
54
55
56 [100] LAMMPS - a flexible simulation tool for particle-based materials modeling at the atomic, meso, and continuum
57 scales, A.P. Thompson, H.M. Aktulga, R. Berger, D.S. Bolintineanu, W.M. Brown, P.S. Crozier, P.J. in 't Veld,
58
59
60
61
62
63
64
65

1
2
3
4
5
6
7
8
9
10
11
12
13
14
15
16
17
18
19
20
21
22
23
24
25
26
27
28
29
30
31
32
33
34
35
36
37
38
39
40
41
42
43
44
45
46
47
48
49
50
51
52
53
54
55
56
57
58
59
60
61
62
63
64
65

A. Kohlmeyer, S.G. Moore, T. D. Nguyen, R. Shan, M.J. Stevens, J. Tranchida, C. Trott, S.J. Plimpton, Comp. Phys. Comm. 271 (2022) 10817.

1
2
3
4
5
6
7
8
9
10
11
12
13
14
15
16
17
18
19
20
21
22
23
24
25
26
27
28
29
30
31
32
33
34
35
36
37
38
39
40
41
42
43
44
45
46
47
48
49
50
51
52
53
54
55
56
57
58
59
60
61
62
63
64
65

Algorithm 1. Algorithm for morphology simulation and mesh generation of particulate composite microstructures

(i) Step 1: Initialize

(i.a) Set $\beta_1, \beta_2, \mu, \Delta_1, \Delta_2$, and RVE size

(ii) Step 2: Generate inclusion microstructure

(ii.a) Construct 2D rectangular grids over $[0, \pi] \times [0, 2\pi]$

(ii.b) Generate stationary Gaussian random field for the coarse-scale inclusion microstructure

(ii.c) Generate fractional Brownian random field for the fine-scale inclusion microstructure

(ii.d) Smooth the coupled coarse-scale and fine-scale inclusion microstructures

(ii.e) Extract morphological parameters from real particulate inclusion database

(ii.f) Utilize the proposed multi-cut method to obtain 2D shape profiles of the generated inclusion microstructure

(ii.g) Check the morphological parameters of computed inclusion shape profiles. IF the parameters are satisfied,

THEN go to Step 3, ELSE go to Substep ii.b

(iii) Step 3: Generate RVE microstructure

(iii.a) Generate non-intersecting spheres

(iii.b) Extract the centers of the spheres generated in Substep iii.a

(iii.c) Use the sphere centers in Substep iii.b as the initial seeds to generate Voronoi cells for the RVE

(iii.d) Use scaling, subdivision, and fusion to place the generated inclusions in the RVE cells

(iii.e) Check the cell filling condition. IF all the generated inclusions have been successfully placed in the RVE,

THEN go to Step 4, ELSE go to Substep iii.d

(iv) Step 4: Generate RVE mesh

(iv.a) Compute the initial curvature of the generated inclusion microstructure in the RVE cell

(iv.b) Perform surface smoothing and compute the curvature of the smoothed inclusion microstructure

(iv.c) Check the surface mesh smoothing criterion. IF the surface mesh is satisfied, THEN go to Substep iv.d,

ELSE go to Substep iv.b.

(iv.d) Generate the volume mesh based on the surface mesh generated in Substep iv.c

(iv.e) Check the volume mesh local refinement criterion. IF the volume mesh is satisfied, THEN go to Substep

iv.b, ELSE go to Step 5.

(v) Step 5: Return the generated RVE microstructure and the relevant mesh

1
2
3
4
5
6
7
8
9
10
11
12
13
14
15
16
17
18
19
20
21
22
23
24
25
26
27
28
29
30
31
32
33
34
35
36
37
38
39
40
41
42
43
44
45
46
47
48
49
50
51
52
53
54
55
56
57
58
59
60
61
62
63
64
65

Table 1. Summary of important articles relating to the advanced modeling approaches for generating 3D particulate geo-microstructures

Article [Ref. No.]	Approach for 3D geo-microstructure generation	Comments
Mollon and Zhao [16]	Fourier descriptors based on Fourier series	Mesh generation is not discussed.
Garboczi et al. [17, 18]	Spherical harmonics	Mesh generation is not discussed.
Zhou et al. [19, 20]	Spherical harmonics	Mesh generation is not discussed.
Huang et al. [23]	Alpha shape	Mesh generation is not discussed.

1
2
3
4
5
6
7
8
9
10
11
12
13
14
15
16
17
18
19
20
21
22
23
24
25
26
27
28
29
30
31
32
33
34
35
36
37
38
39
40
41
42
43
44
45
46
47
48
49
50
51
52
53
54
55
56
57
58
59
60
61
62
63
64
65

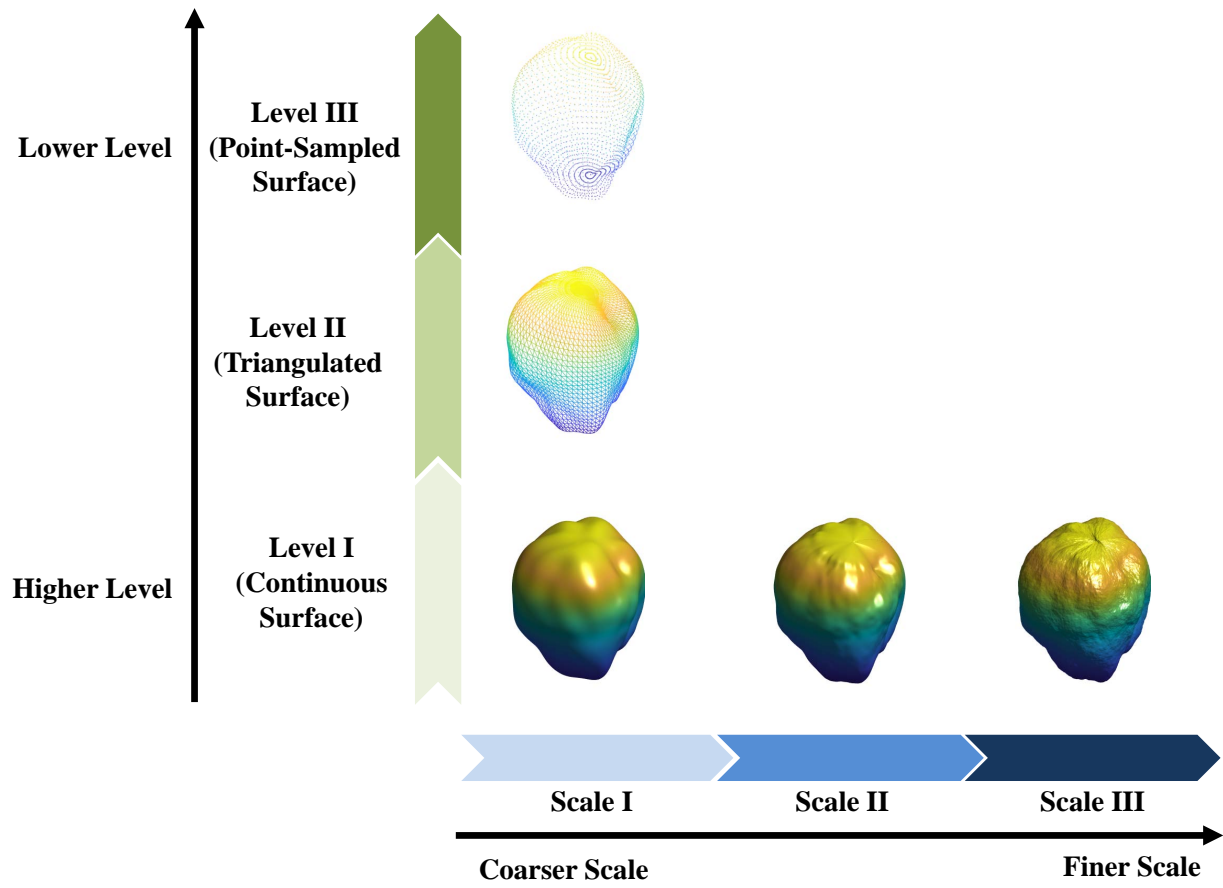


Figure 1: Schematic illustration of the proposed multiscale multi-level representation scheme.

1
2
3
4
5
6
7
8
9
10
11
12
13
14
15
16
17
18
19
20
21
22
23
24
25
26
27
28
29
30
31
32
33
34
35
36
37
38
39
40
41
42
43
44
45
46
47
48
49
50
51
52
53
54
55
56
57
58
59
60
61
62
63
64
65

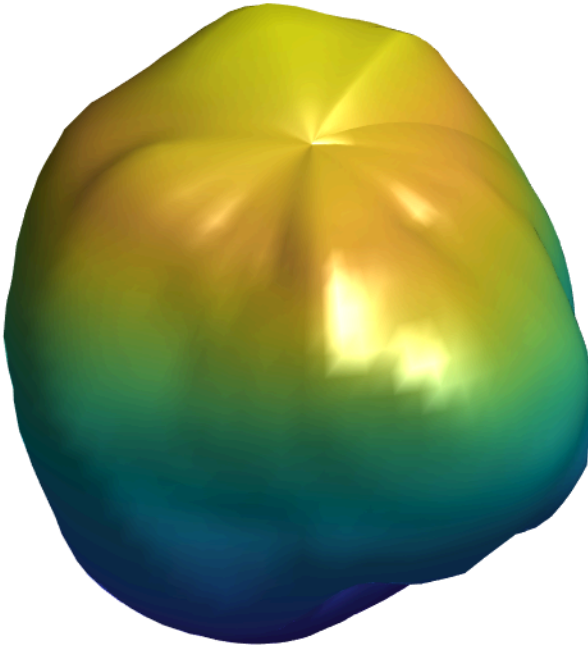
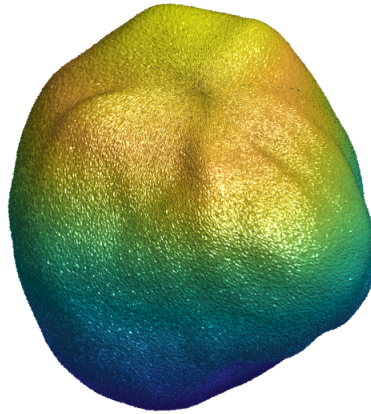


Figure 2: Illustration of the proposed coarse-scale simulation procedure.

1
2
3
4
5
6
7
8
9
10
11
12
13
14
15
16
17
18
19
20
21
22
23
24
25
26
27
28
29
30
31
32
33
34
35
36
37
38
39
40
41
42
43
44
45
46
47
48
49
50
51
52
53
54
55
56
57
58
59
60
61
62
63
64
65

(a) approach by using random noise



(b) approach by using fractional Brownian random field

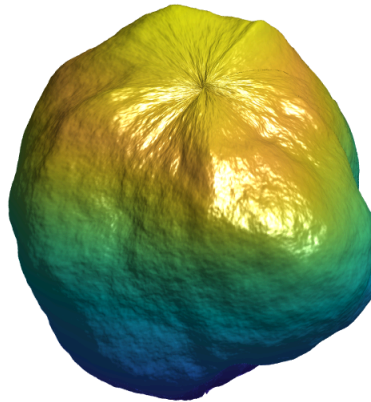


Figure 3: Illustration of the proposed fine-scale simulation procedure: (a) approach by using random noise; (b) approach by using fractional Brownian random field.

1
2
3
4
5
6
7
8
9
10
11
12
13
14
15
16
17
18
19
20
21
22
23
24
25
26
27
28
29
30
31
32
33
34
35
36
37
38
39
40
41
42
43
44
45
46
47
48
49
50
51
52
53
54
55
56
57
58
59
60
61
62
63
64
65

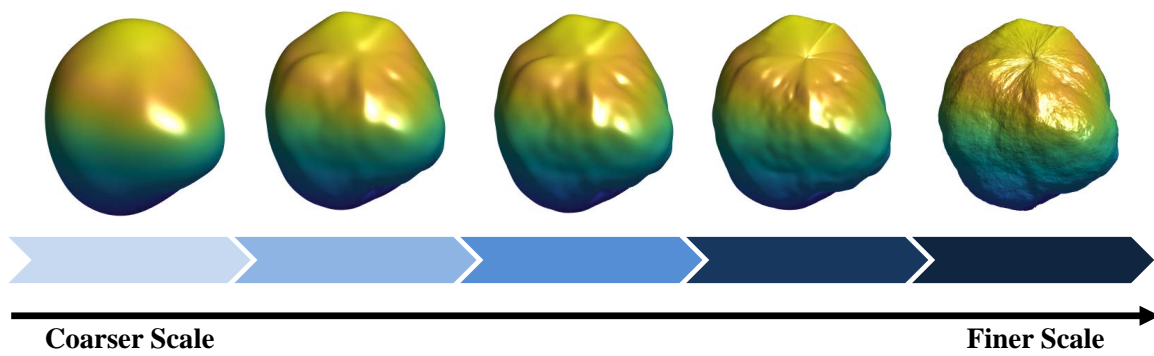


Figure 4: Illustration of the proposed multiscale heat kernel smoothing scheme for bridging the coarse and fine scales.

1
2
3
4
5
6
7
8
9
10
11
12
13
14
15
16
17
18
19
20
21
22
23
24
25
26
27
28
29
30
31
32
33
34
35
36
37
38
39
40
41
42
43
44
45
46
47
48
49
50
51
52
53
54
55
56
57
58
59
60
61
62
63
64
65

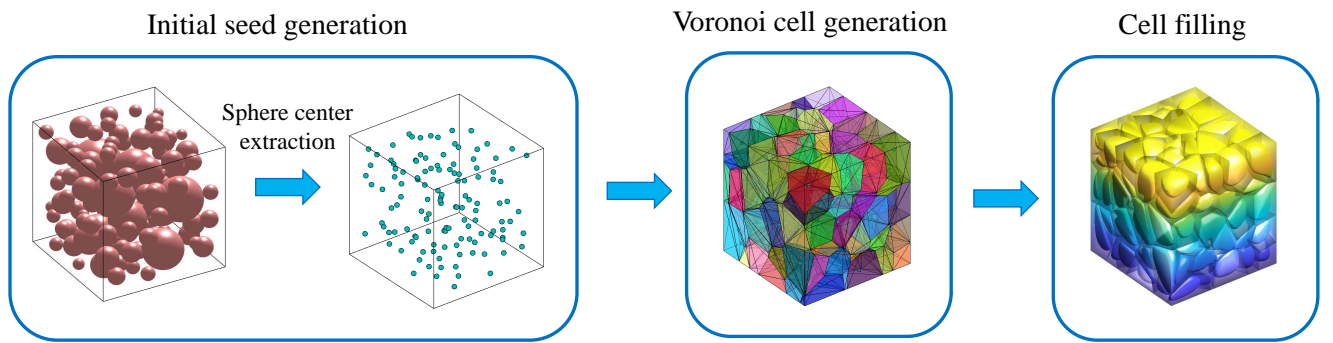


Figure 5: Illustration of the proposed RVE generation procedure.

1
2
3
4
5
6
7
8
9
10
11
12
13
14
15
16
17
18
19
20
21
22
23
24
25
26
27
28
29
30
31
32
33
34
35
36
37
38
39
40
41
42
43
44
45
46
47
48
49
50
51
52
53
54
55
56
57
58
59
60
61
62
63
64
65

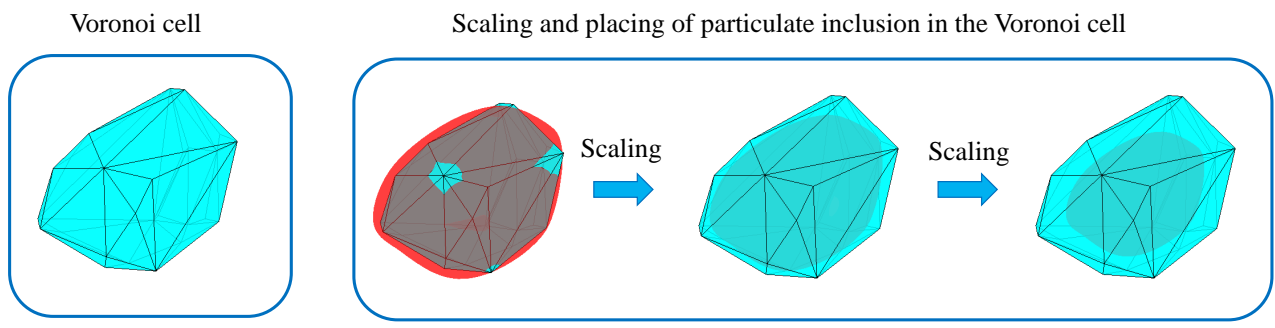


Figure 6: Illustration of the proposed scaling operation in the cell filling process.

1
2
3
4
5
6
7
8
9
10
11
12
13
14
15
16
17
18
19
20
21
22
23
24
25
26
27
28
29
30
31
32
33
34
35
36
37
38
39
40
41
42
43
44
45
46
47
48
49
50
51
52
53
54
55
56
57
58
59
60
61
62
63
64
65

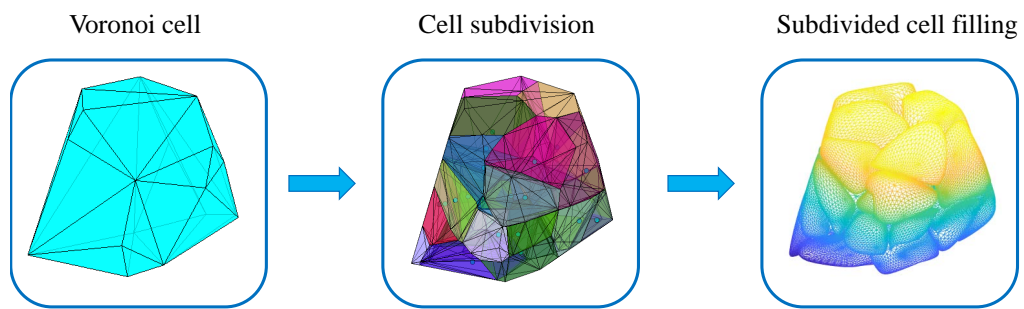


Figure 7: Illustration of the proposed subdivision operation in the cell filling process.

1
2
3
4
5
6
7
8
9
10
11
12
13
14
15
16
17
18
19
20
21
22
23
24
25
26
27
28
29
30
31
32
33
34
35
36
37
38
39
40
41
42
43
44
45
46
47
48
49
50
51
52
53
54
55
56
57
58
59
60
61
62
63
64
65

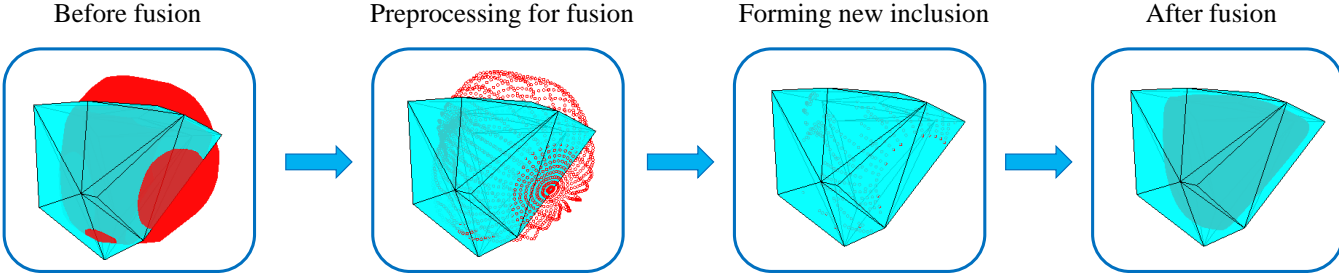
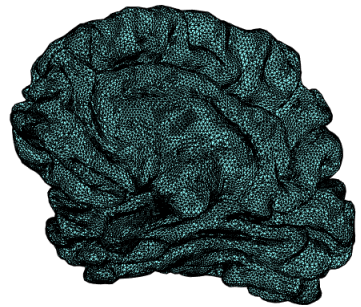


Figure 8: Illustration of the proposed fusion operation in the cell filling process.

1
2
3
4
5
6
7
8
9
10
11
12
13
14
15
16
17
18
19
20
21
22
23
24
25
26
27
28
29
30
31
32
33
34
35
36
37
38
39
40
41
42
43
44
45
46
47
48
49
50
51
52
53
54
55
56
57
58
59
60
61
62
63
64
65

(a) cortical surface



(b) parametrized surface

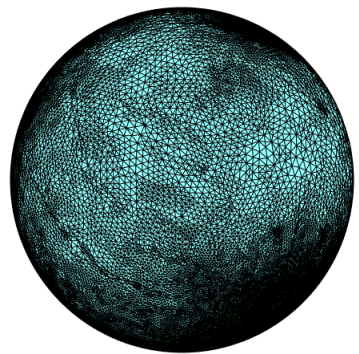


Figure 9: Illustration of the surface parametrization procedure adopted in the present study: (a) cortical surface;
(b) parametrized surface.

1
2
3
4
5
6
7
8
9
10
11
12
13
14
15
16
17
18
19
20
21
22
23
24
25
26
27
28
29
30
31
32
33
34
35
36
37
38
39
40
41
42
43
44
45
46
47
48
49
50
51
52
53
54
55
56
57
58
59
60
61
62
63
64
65

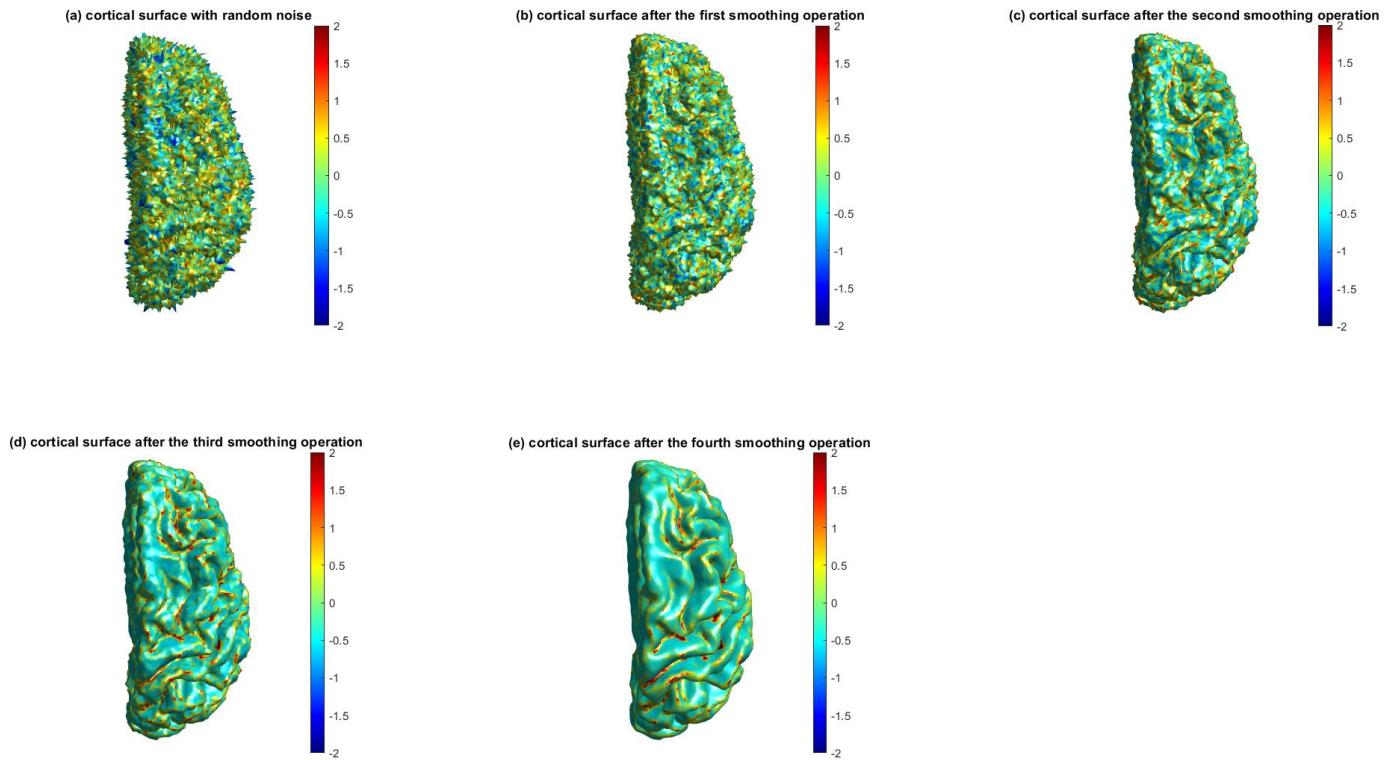
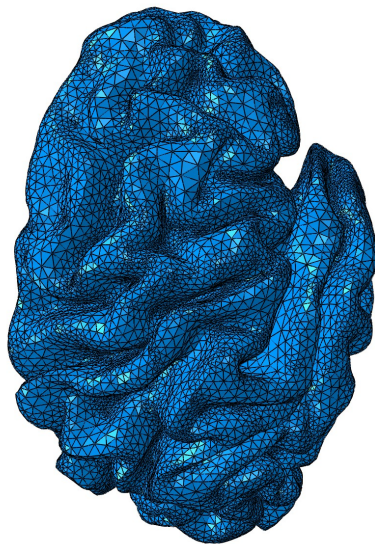


Figure 10: Illustration of the proposed curvature-based surface mesh generation procedure for the smoothing and generation of the cortical surface mesh: (a) cortical surface with random noise; (b) cortical surface after the first smoothing operation; (c) cortical surface after the second smoothing operation; (d) cortical surface after the third smoothing operation; (e) cortical surface after the fourth smoothing operation.

1
2
3
4
5
6
7
8
9
10
11
12
13
14
15
16
17
18
19
20
21
22
23
24
25
26
27
28
29
30
31
32
33
34
35
36
37
38
39
40
41
42
43
44
45
46
47
48
49
50
51
52
53
54
55
56
57
58
59
60
61
62
63
64
65

(a) volume mesh



(b) cut volume mesh

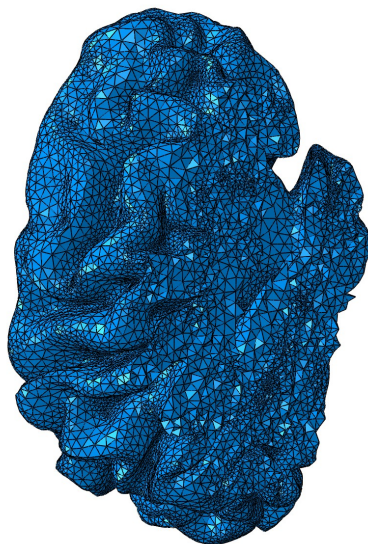


Figure 11: Illustration of the generation of the volume mesh for the cortical surface in Figure 10e: (a) volume mesh; (b) cut volume mesh.

1
2
3
4
5
6
7
8
9
10
11
12
13
14
15
16
17
18
19
20
21
22
23
24
25
26
27
28
29
30
31
32
33
34
35
36
37
38
39
40
41
42
43
44
45
46
47
48
49
50
51
52
53
54
55
56
57
58
59
60
61
62
63
64
65

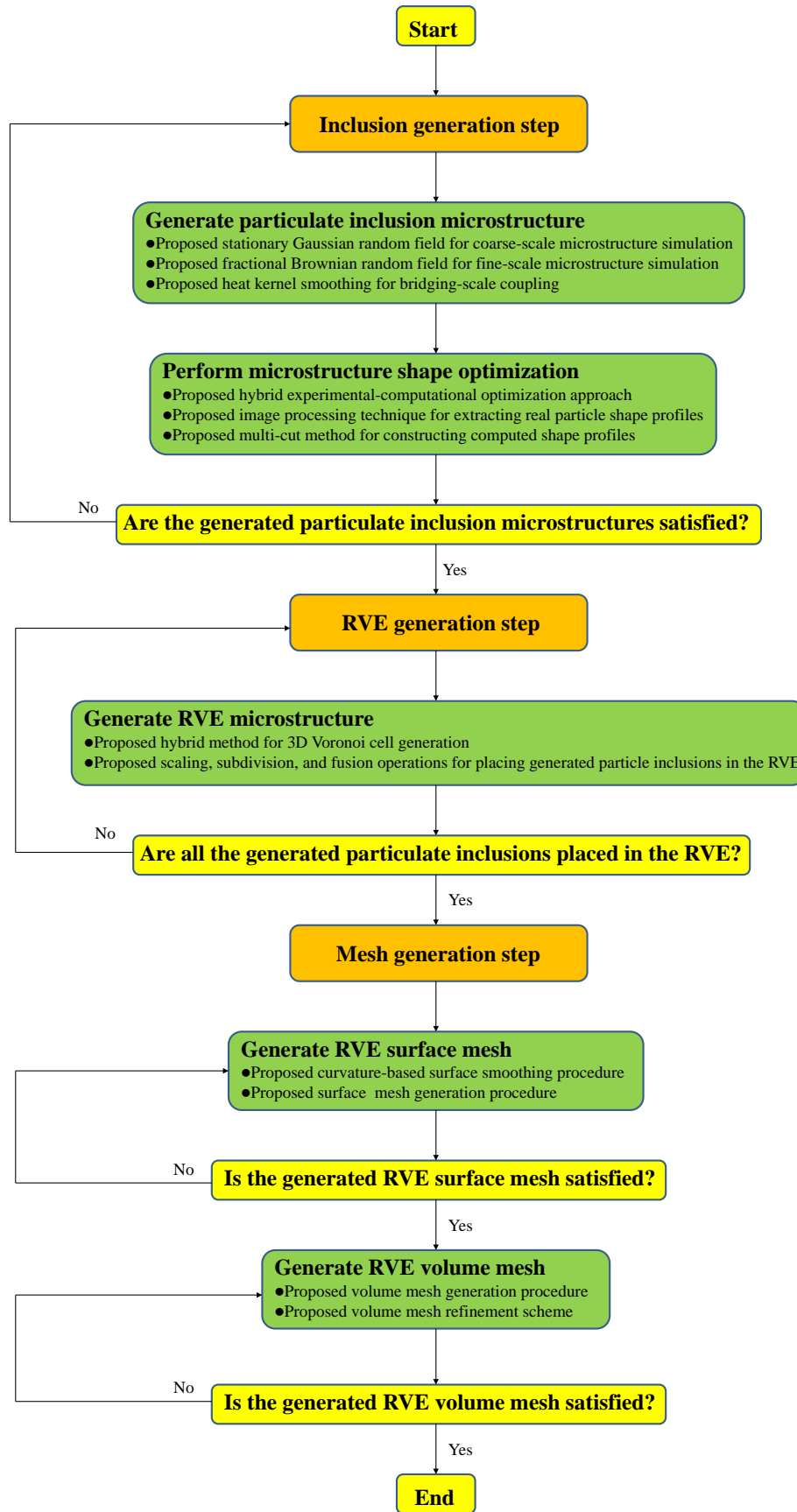
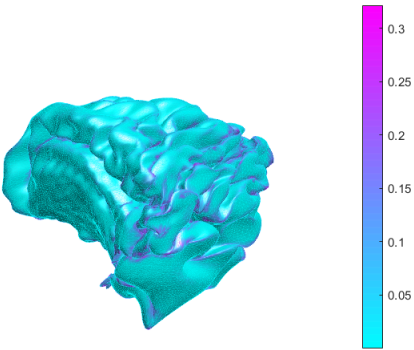


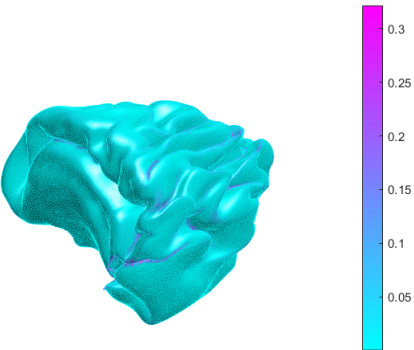
Figure 12: Flowchart of the complete computational framework proposed in the present study.

1
2
3
4
5
6
7
8
9
10
11
12
13
14
15
16
17
18
19
20
21
22
23
24
25
26
27
28
29
30
31
32
33
34
35
36
37
38
39
40
41
42
43
44
45
46
47
48
49
50
51
52
53
54
55
56
57
58
59
60
61
62
63
64
65

(a) cortical surface smoothed using $t=0$



(b) cortical surface smoothed using $t=0.001$



(c) cortical surface smoothed using $t=0.01$

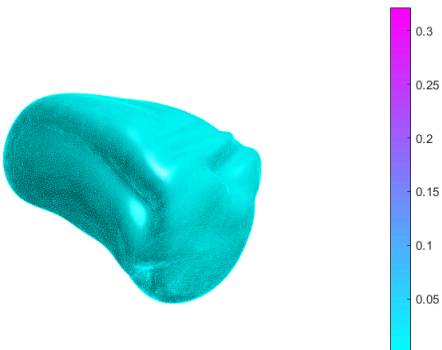


Figure 13: Illustration of the weighted spherical harmonic smoothing and surface flattening of the cortical surface:

(a) cortical surface smoothed using $t=0$; (b) cortical surface smoothed using $t=0.001$; (c) cortical surface smoothed using $t=0.01$.

1
2
3
4
5
6
7
8
9
10
11
12
13
14
15
16
17
18
19
20
21
22
23
24
25
26
27
28
29
30
31
32
33
34
35
36
37
38
39
40
41
42
43
44
45
46
47
48
49
50
51
52
53
54
55
56
57
58
59
60
61
62
63
64
65

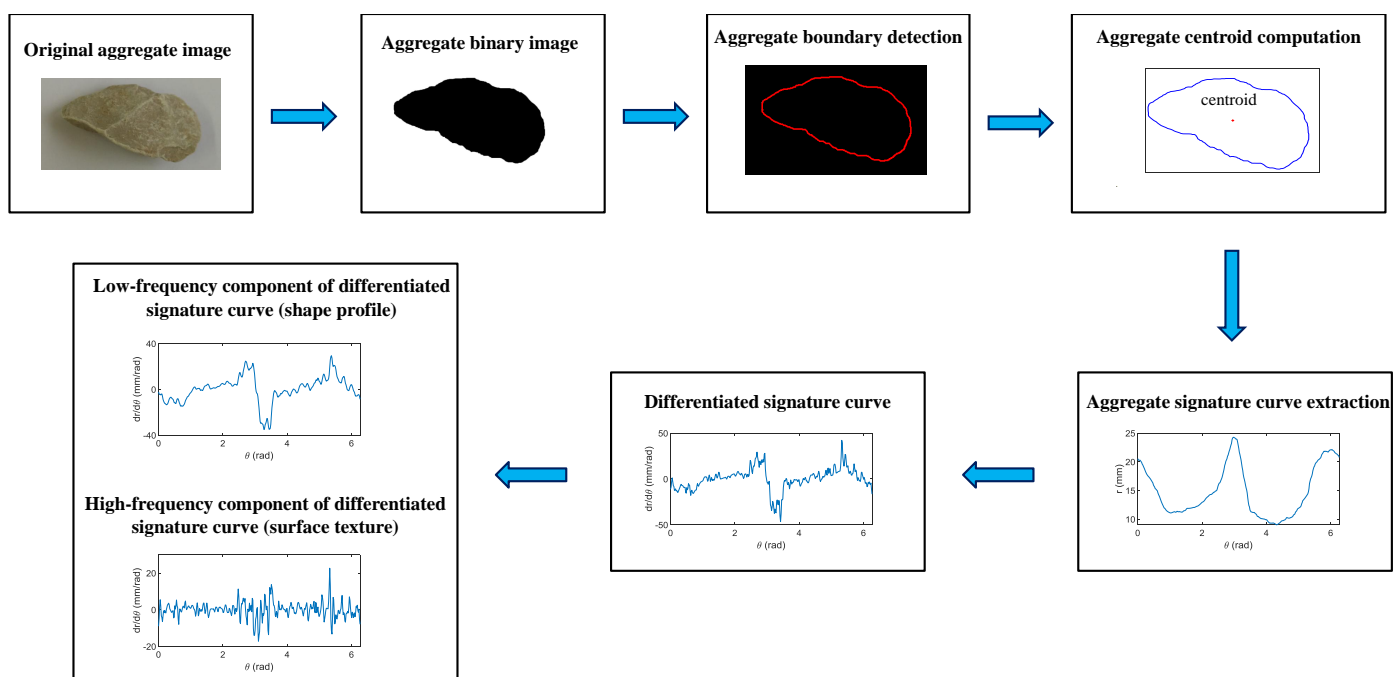
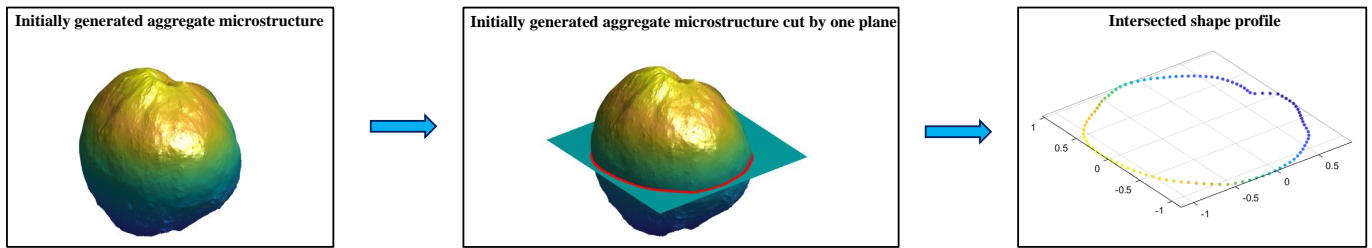


Figure 14: Illustration of the image processing procedure for extracting particle shape profile.

1
2
3
4
5
6
7
8
9
10
11
12
13
14
15
16
17
18
19
20
21
22
23
24
25
26
27
28
29
30
31
32
33
34
35
36
37
38
39
40
41
42
43
44
45
46
47
48
49
50
51
52
53
54
55
56
57
58
59
60
61
62
63
64
65

(a) method for obtaining intersected particle shape profile



(b) shape optimization procedure using multiple plane cuts

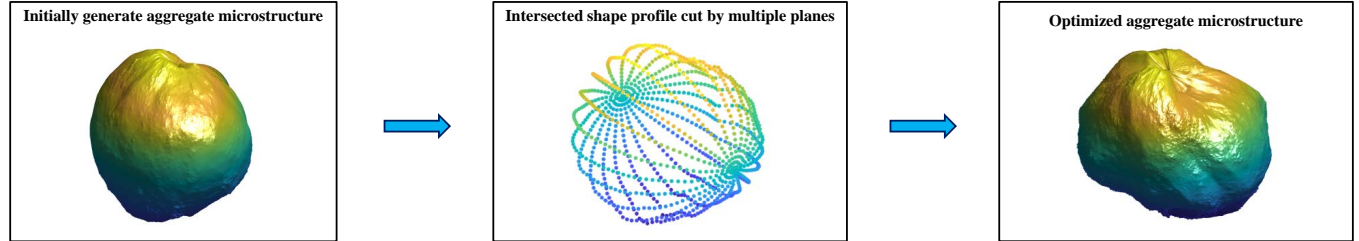
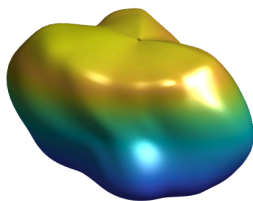


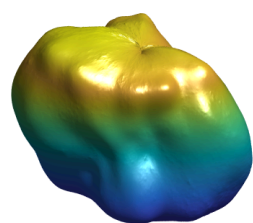
Figure 15: Illustration of the proposed microstructural shape optimization procedure: (a) method for obtaining intersected particle shape profile; (b) shape optimization procedure using multiple plane cuts.

1
2
3
4
5
6
7
8
9
10
11
12
13
14
15
16
17
18
19
20
21
22
23
24
25
26
27
28
29
30
31
32
33
34
35
36
37
38
39
40
41
42
43
44
45
46
47
48
49
50
51
52
53
54
55
56
57
58
59
60
61
62
63
64
65

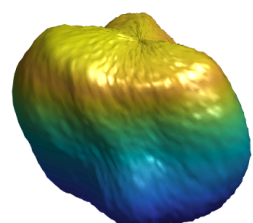
(a) no surface texture



(b) mild surface texture



(c) medium surface texture



(d) strong surface texture

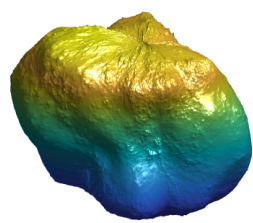
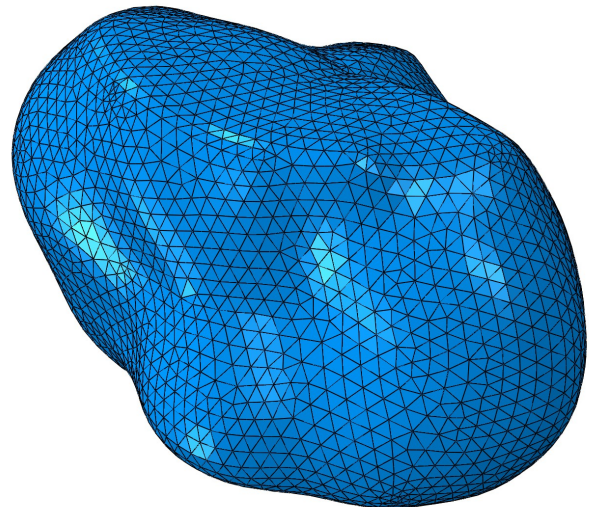


Figure 16: Generation of aggregate microstructures with different surface texture: (a) no surface texture; (b) mild surface texture; (c) medium surface texture; (d) strong surface texture.

1
2
3
4
5
6
7
8
9
10
11
12
13
14
15
16
17
18
19
20
21
22
23
24
25
26
27
28
29
30
31
32
33
34
35
36
37
38
39
40
41
42
43
44
45
46
47
48
49
50
51
52
53
54
55
56
57
58
59
60
61
62
63
64
65

(a) volume mesh



(b) cut volume mesh

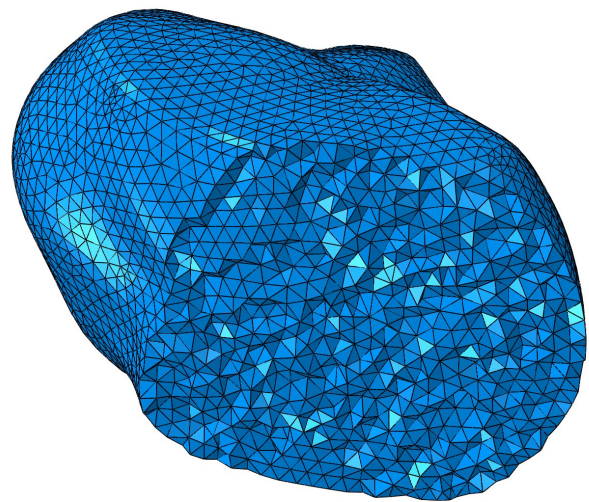
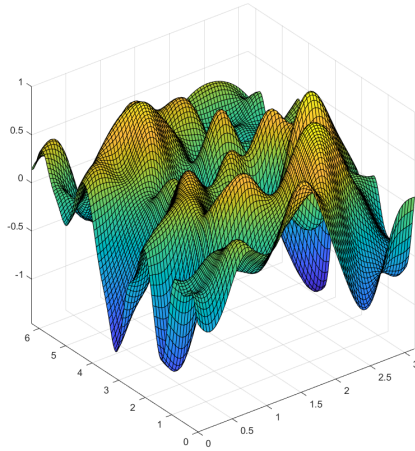
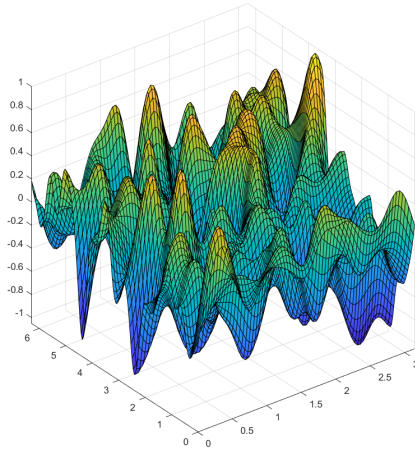


Figure 17: Volume Mesh for smoothed aggregate microstructure of Figure 16: (a) volume mesh; (b) cut volume mesh.

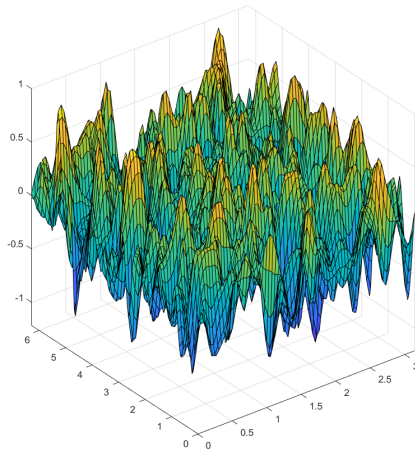
1
2
3 (a) stationary Gaussian random field generated with parameter $\beta_1 = \beta_2 = 1/5$
4
5
6



7
8
9
10
11
12
13
14
15
16
17
18
19
20
21
22 (b) stationary Gaussian random field generated with parameter $\beta_1 = \beta_2 = 1/10$
23
24

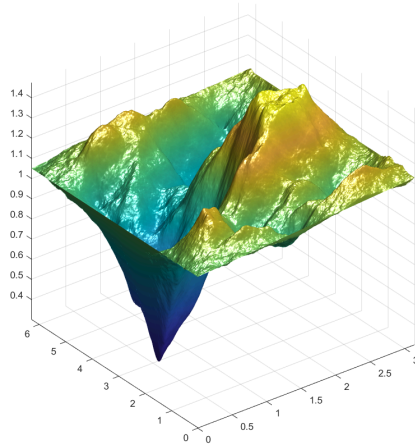


25
26
27
28
29
30
31
32
33
34
35
36
37
38
39
40 (c) stationary Gaussian random field generated with parameter $\beta_1 = \beta_2 = 1/50$
41
42
43

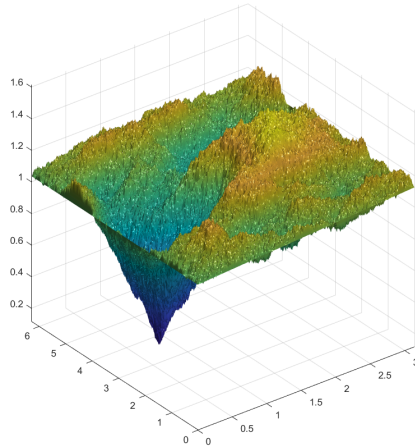


44
45
46
47
48
49
50
51
52
53
54
55
56
57
58
59
60 Figure 18: Effects of the correlation length parameter on the generated random field: (a) stationary Gaussian
61 random field generated with parameter $\beta_1 = \beta_2 = 1/5$; (b) stationary Gaussian random field generated with
62 parameter $\beta_1 = \beta_2 = 1/10$; (c) stationary Gaussian random field generated with parameter $\beta_1 = \beta_2 = 1/50$.
63
64
65

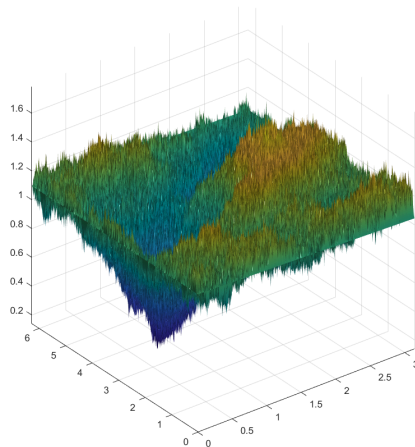
1
2
3 (a) fractional Brownian random field generated with the Hurst parameter $\mu = 0.8$
4
5



21
22 (b) fractional Brownian random field generated with the Hurst parameter $\mu = 0.4$
23
24



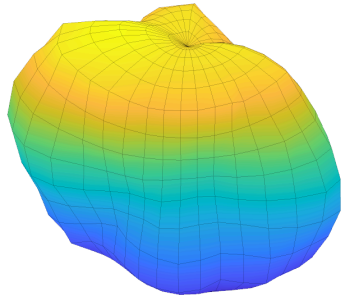
40 (c) fractional Brownian random field generated with the Hurst parameter $\mu = 0.1$
41
42
43



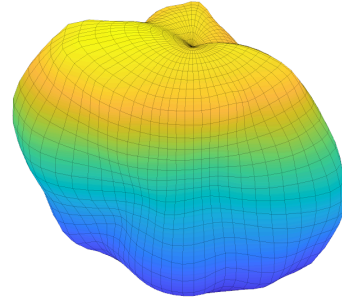
59
60 Figure 19: Effects of the Hurst parameter on the generated random field: (a) fractional Brownian random field
61 generated with the Hurst parameter $\mu = 0.8$; (b) fractional Brownian random field generated with the Hurst
62 parameter $\mu = 0.4$; (c) fractional Brownian random field generated with the Hurst parameter $\mu = 0.1$.
63
64
65

1
2
3
4
5
6
7
8
9
10
11
12
13
14
15
16
17
18
19
20
21
22
23
24
25
26
27
28
29
30
31
32
33
34
35
36
37
38
39
40
41
42
43
44
45
46
47
48
49
50
51
52
53
54
55
56
57
58
59
60
61
62
63
64
65

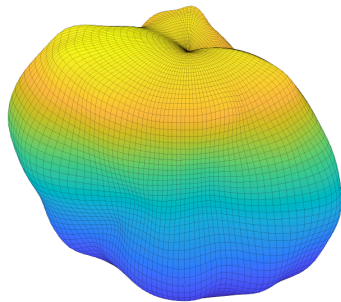
(a) grid spacing $\Delta_1 = \Delta_2 = \pi/18$



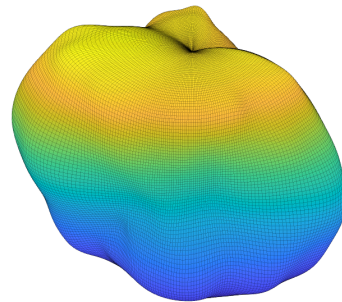
(b) grid spacing $\Delta_1 = \Delta_2 = \pi/36$



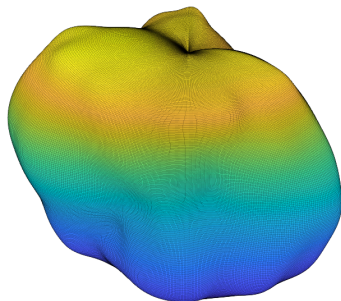
(c) grid spacing $\Delta_1 = \Delta_2 = \pi/72$



(d) grid spacing $\Delta_1 = \Delta_2 = \pi/144$



(e) grid spacing $\Delta_1 = \Delta_2 = \pi/288$



(f) grid spacing $\Delta_1 = \Delta_2 = \pi/512$

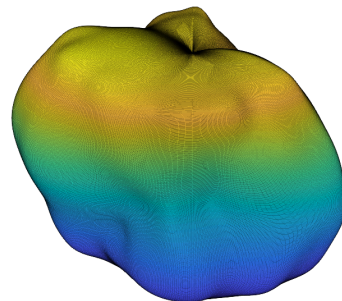


Figure 20: Effects of grid spacing on the generated microstructure: (a) grid spacing $\Delta_1 = \Delta_2 = \pi/18$; (b) grid spacing $\Delta_1 = \Delta_2 = \pi/36$; (c) grid spacing $\Delta_1 = \Delta_2 = \pi/72$; (d) grid spacing $\Delta_1 = \Delta_2 = \pi/144$; (e) grid spacing $\Delta_1 = \Delta_2 = \pi/288$; (f) grid spacing $\Delta_1 = \Delta_2 = \pi/512$.

1
2
3
4
5
6
7
8
9
10
11
12
13
14
15
16
17
18
19
20
21
22
23
24
25
26
27
28
29
30
31
32
33
34
35
36
37
38
39
40
41
42
43
44
45
46
47
48
49
50
51
52
53
54
55
56
57
58
59
60
61
62
63
64
65

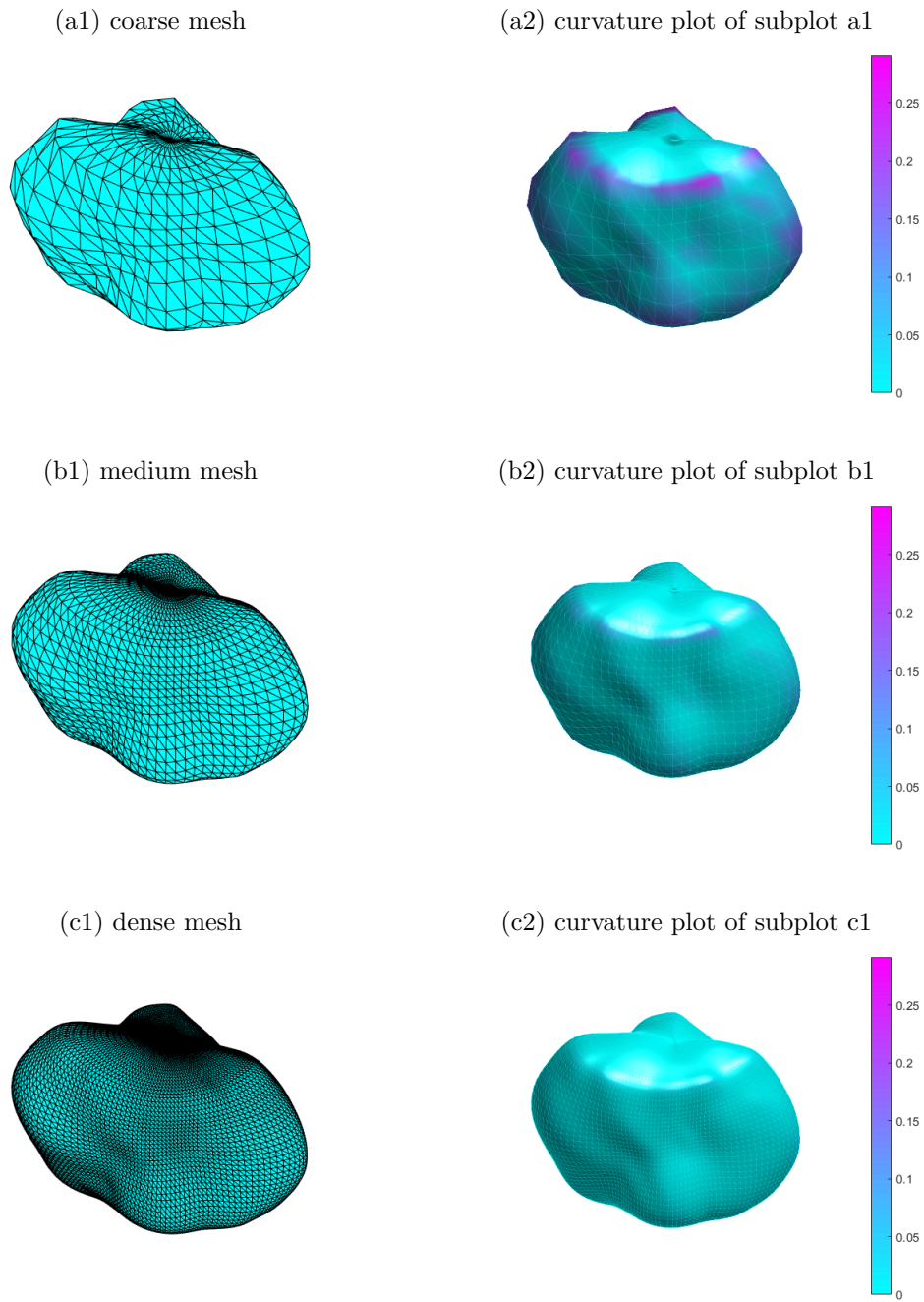
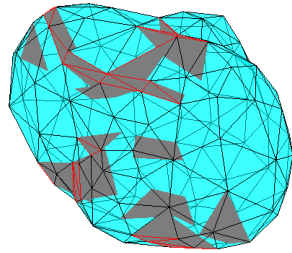


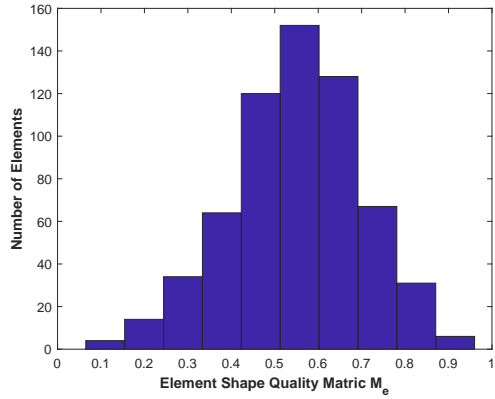
Figure 21: Refined surface meshes of the aggregate microstructure: (a1) coarse mesh; (a2) curvature plot of subplot a1; (b1) medium mesh; (b2) curvature plot of subplot b1; (c1) dense mesh; (c2) curvature plot of subplot c1.

1
2
3
4
5
6
7
8
9
10
11
12
13
14
15
16
17
18
19
20
21
22
23
24
25
26
27
28
29
30
31
32
33
34
35
36
37
38
39
40
41
42
43
44
45
46
47
48
49
50
51
52
53
54
55
56
57
58
59
60
61
62
63
64
65

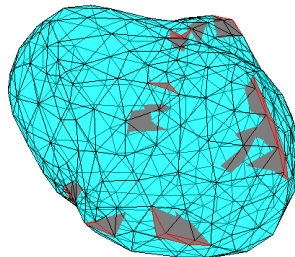
(a1) initial mesh



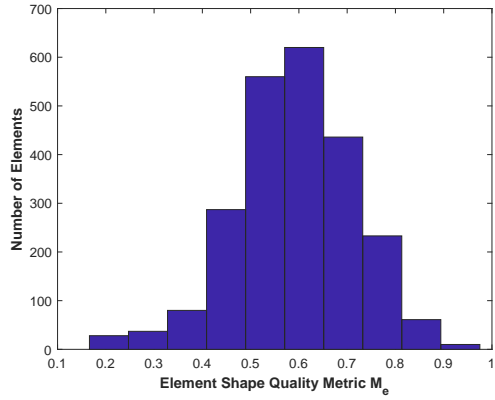
(a2) element shape quality for subplot a1



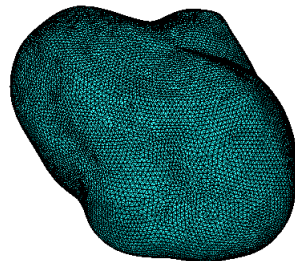
(b1) mesh refined from subplot a1



(b2) element shape quality for subplot b1



(c1) mesh refined from subplot b1



(c2) element shape quality for subplot c1

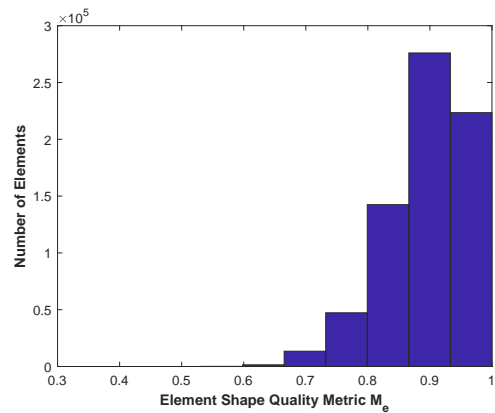
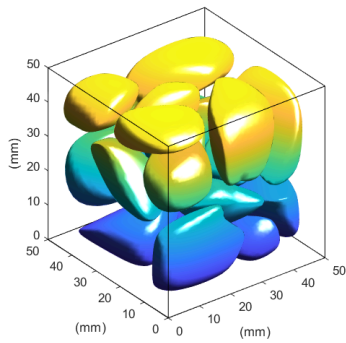


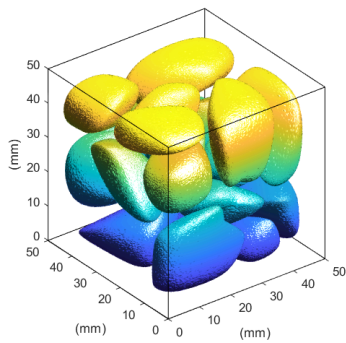
Figure 22: Refined volume meshes and element quality statistics of the aggregate microstructure: (a1) initial mesh; (a2) element shape quality for subplot a1; (b1) mesh refined from subplot a1; (b2) element shape quality for subplot b1; (c1) mesh refined from subplot b1; (a2) element shape quality for subplot c1. Note that in the figure, the elements with poor quality are highlighted in red.

1
2
3
4
5
6
7
8
9
10
11
12
13
14
15
16
17
18
19
20
21
22
23
24
25
26
27
28
29
30
31
32
33
34
35
36
37
38
39
40
41
42
43
44
45
46
47
48
49
50
51
52
53
54
55
56
57
58
59
60
61
62
63
64
65

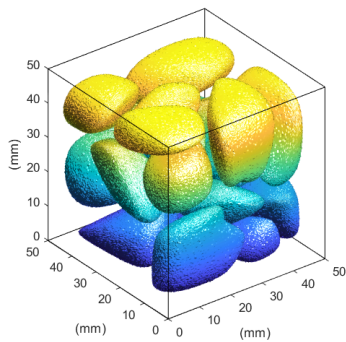
(a) no surface texture



(b) mild surface texture



(c) medium surface texture



(d) strong surface texture

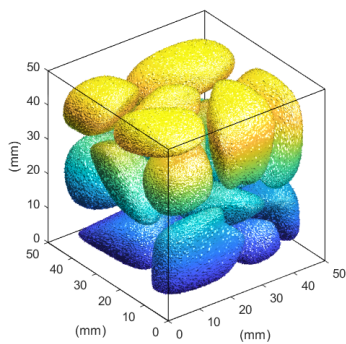
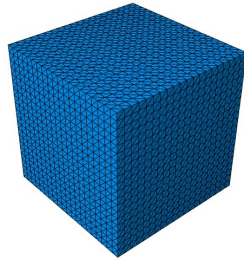


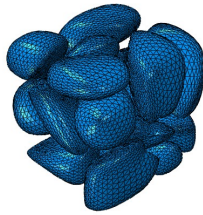
Figure 23: Generation of cementitious composite microstructures with different surface texture (scenario with low packing density and regular shape): (a) no surface texture; (b) mild surface texture; (c) medium surface texture; (d) strong surface texture.

1
2
3
4
5
6
7
8
9
10
11
12
13
14
15
16
17
18
19
20
21
22
23
24
25
26
27
28
29
30
31
32
33
34
35
36
37
38
39
40
41
42
43
44
45
46
47
48
49
50
51
52
53
54
55
56
57
58
59
60
61
62
63
64
65

(a) RVE



(b) aggregate



(c) cut aggregate



(d) cut matrix

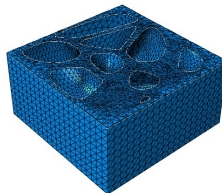
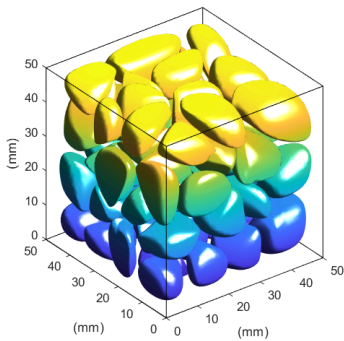


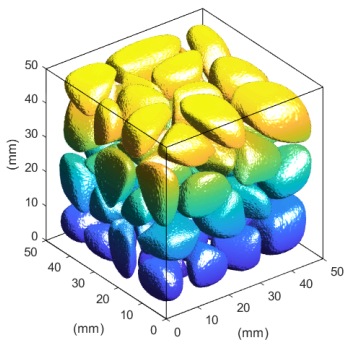
Figure 24: Volume mesh for smoothed cementitious composite microstructures for the RVE shown in Figure 23:
(a) RVE; (b) aggregate; (c) cut aggregate; (d) cut matrix.

1
2
3
4
5
6
7
8
9
10
11
12
13
14
15
16
17
18
19
20
21
22
23
24
25
26
27
28
29
30
31
32
33
34
35
36
37
38
39
40
41
42
43
44
45
46
47
48
49
50
51
52
53
54
55
56
57
58
59
60
61
62
63
64
65

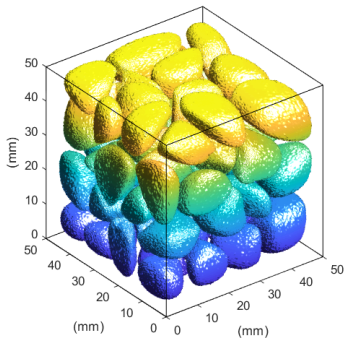
(a) no surface texture



(b) mild surface texture



(c) medium surface texture



(d) strong surface texture

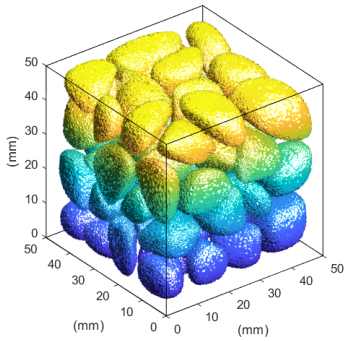
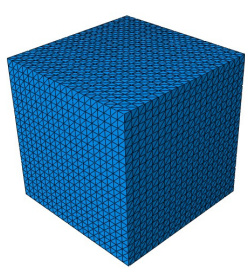


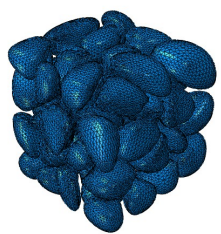
Figure 25: Generation of cementitious composite microstructures with different surface texture (scenario with high packing density and regular shape): (a) no surface texture; (b) mild surface texture; (c) medium surface texture; (d) strong surface texture.

1
2
3
4
5
6
7
8
9
10
11
12
13
14
15
16
17
18
19
20
21
22
23
24
25
26
27
28
29
30
31
32
33
34
35
36
37
38
39
40
41
42
43
44
45
46
47
48
49
50
51
52
53
54
55
56
57
58
59
60
61
62
63
64
65

(a) RVE



(b) aggregate



(c) cut aggregate



(d) cut matrix

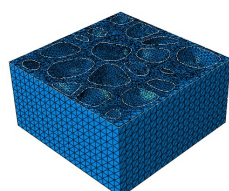
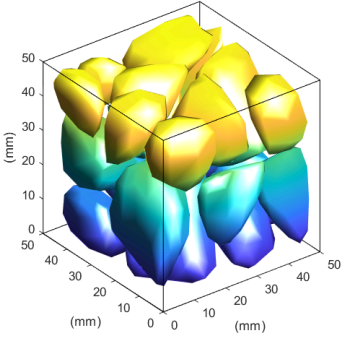


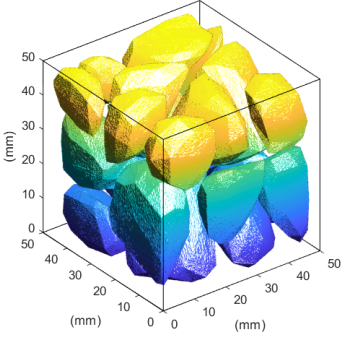
Figure 26: Volume mesh for smoothed cementitious composite microstructures for the RVE shown in Figure 25:
(a) RVE; (b) aggregate; (c) cut aggregate; (d) cut matrix.

1
2
3
4
5
6
7
8
9
10
11
12
13
14
15
16
17
18
19
20
21
22
23
24
25
26
27
28
29
30
31
32
33
34
35
36
37
38
39
40
41
42
43
44
45
46
47
48
49
50
51
52
53
54
55
56
57
58
59
60
61
62
63
64
65

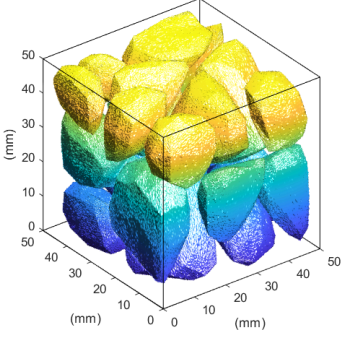
(a) no surface texture



(b) mild surface texture



(c) medium surface texture



(d) strong surface texture

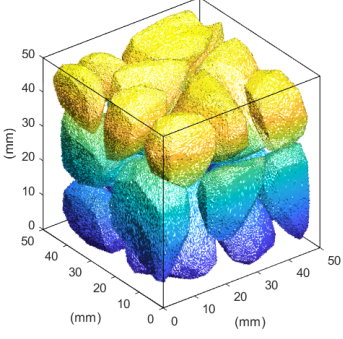
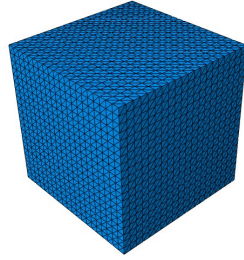


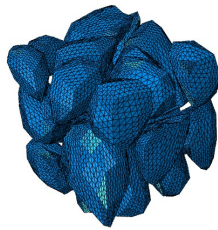
Figure 27: Generation of cementitious composite microstructures with different surface texture (scenario with low packing density and irregular shape): (a) no surface texture; (b) mild surface texture; (c) medium surface texture; (d) strong surface texture.

1
2
3
4
5
6
7
8
9
10
11
12
13
14
15
16
17
18
19
20
21
22
23
24
25
26
27
28
29
30
31
32
33
34
35
36
37
38
39
40
41
42
43
44
45
46
47
48
49
50
51
52
53
54
55
56
57
58
59
60
61
62
63
64
65

(a) RVE



(b) aggregate



(c) cut aggregate



(d) cut matrix

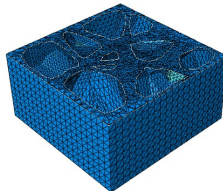
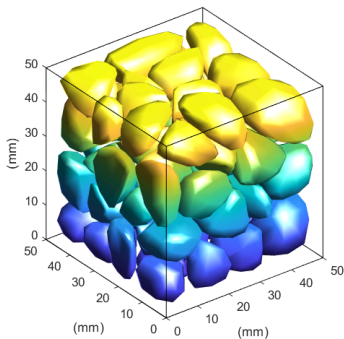


Figure 28: Volume mesh for smoothed cementitious composite microstructures for the RVE shown in Figure 27:

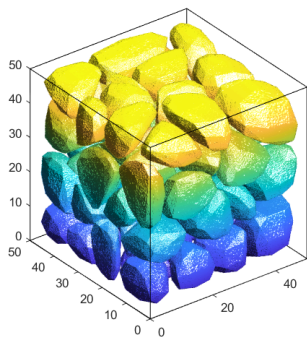
(a) RVE; (b) aggregate; (c) cut aggregate; (d) cut matrix.

1
2
3
4
5
6
7
8
9
10
11
12
13
14
15
16
17
18
19
20
21
22
23
24
25
26
27
28
29
30
31
32
33
34
35
36
37
38
39
40
41
42
43
44
45
46
47
48
49
50
51
52
53
54
55
56
57
58
59
60
61
62
63
64
65

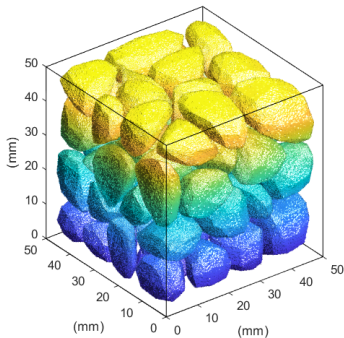
(a) no surface texture



(b) mild surface texture



(c) medium surface texture



(d) strong surface texture

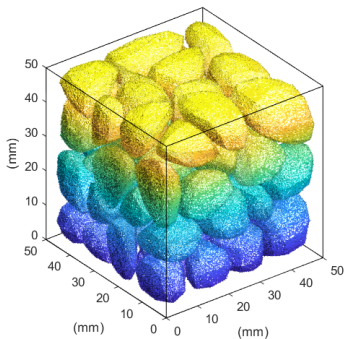
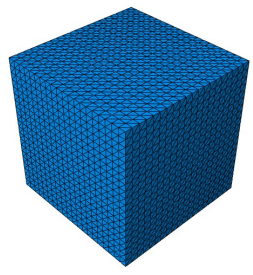


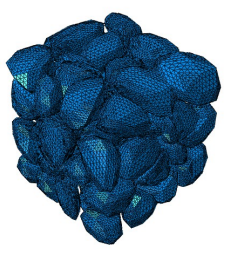
Figure 29: Generation of cementitious composite microstructures with different surface texture (scenario with high packing density and irregular shape): (a) no surface texture; (b) mild surface texture; (c) medium surface texture; (d) strong surface texture.

1
2
3
4
5
6
7
8
9
10
11
12
13
14
15
16
17
18
19
20
21
22
23
24
25
26
27
28
29
30
31
32
33
34
35
36
37
38
39
40
41
42
43
44
45
46
47
48
49
50
51
52
53
54
55
56
57
58
59
60
61
62
63
64
65

(a) RVE



(b) aggregate



(c) cut aggregate



(d) cut matrix

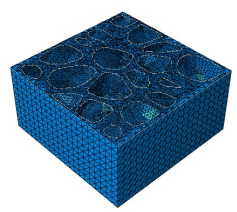


Figure 30: Volume mesh for smoothed cementitious composite microstructures for the RVE shown in Figure 29:
(a) RVE; (b) aggregate; (c) cut aggregate; (d) cut matrix.

1
2
3
4
5
6
7
8
9
10
11
12
13
14
15
16
17
18
19
20
21
22
23
24
25
26
27
28
29
30
31
32
33
34
35
36
37
38
39
40
41
42
43
44
45
46
47
48
49
50
51
52
53
54
55
56
57
58
59
60
61
62
63
64
65

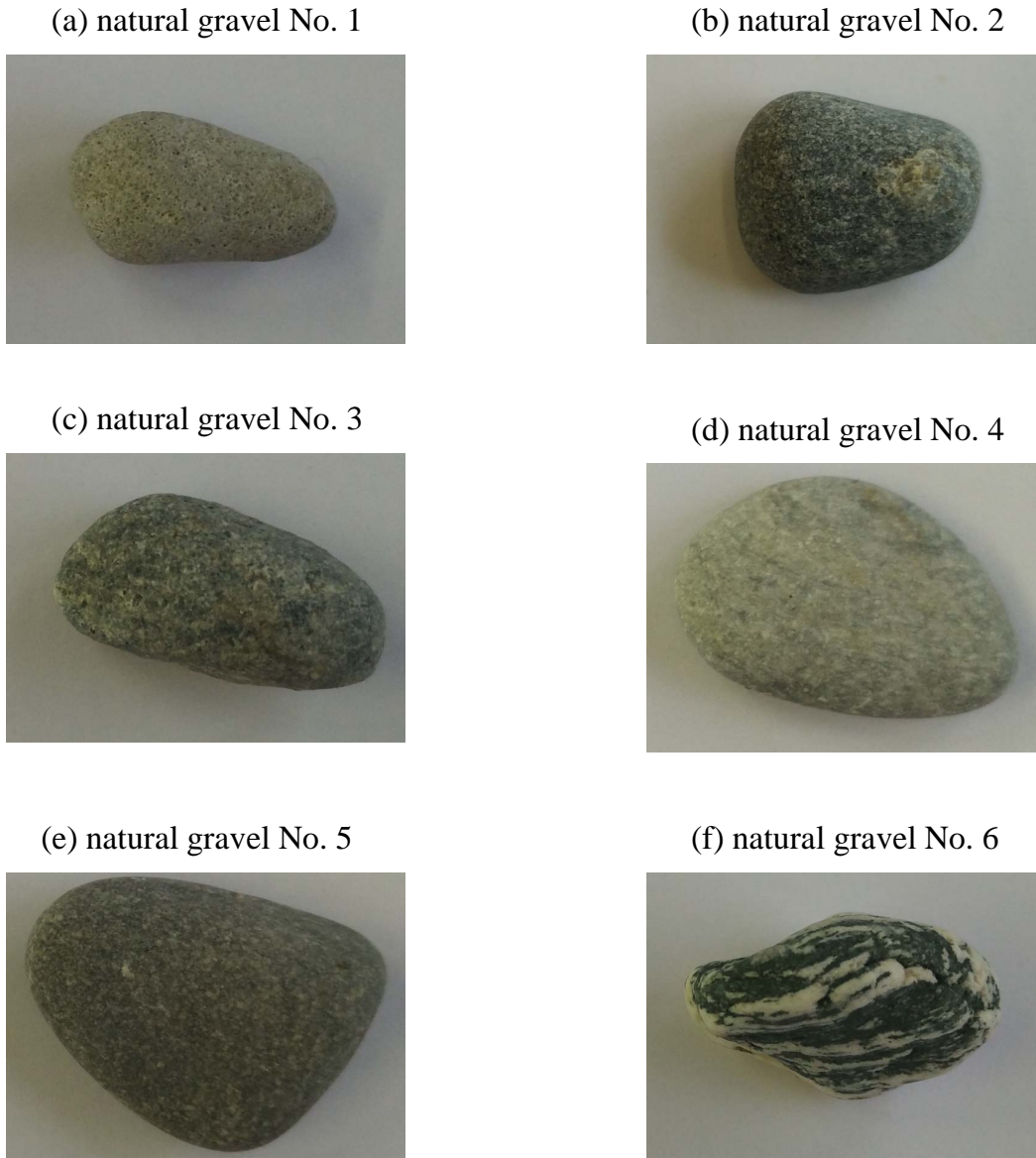
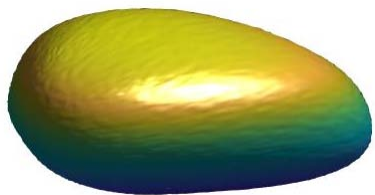


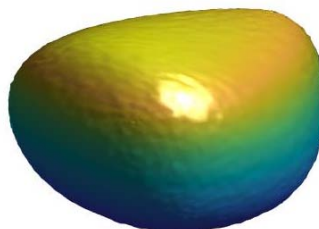
Figure 31: Real natural-gravel-type aggregates: (a) natural gravel No. 1; (b) natural gravel No. 2; (c) natural gravel No. 3; (d) natural gravel No. 4; (e) natural gravel No. 5; (f) natural gravel No. 6.

1
2
3
4
5
6
7
8
9
10
11
12
13
14
15
16
17
18
19
20
21
22
23
24
25
26
27
28
29
30
31
32
33
34
35
36
37
38
39
40
41
42
43
44
45
46
47
48
49
50
51
52
53
54
55
56
57
58
59
60
61
62
63
64
65

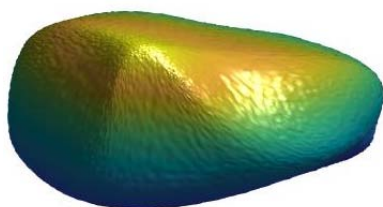
(a) simulated natural gravel No. 1



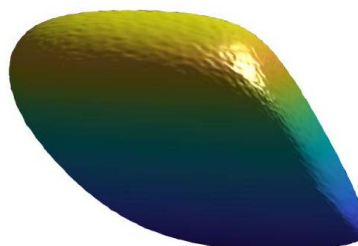
(b) simulated natural gravel No. 2



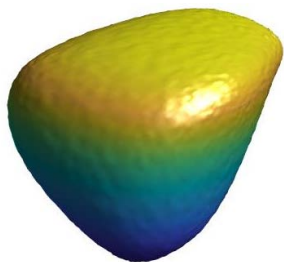
(c) simulated natural gravel No. 3



(d) simulated natural gravel No. 4



(e) simulated natural gravel No. 5



(f) simulated natural gravel No. 6

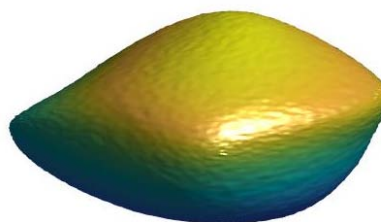


Figure 32: Simulated natural-gravel-type aggregates: (a) simulated natural gravel No. 1; (b) simulated natural gravel No. 2; (c) simulated natural gravel No. 3; (d) simulated natural gravel No. 4; (e) simulated natural gravel No. 5; (f) simulated natural gravel No. 6.

1
2
3
4
5
6
7
8
9
10
11
12
13
14
15
16
17
18
19
20
21
22
23
24
25
26
27
28
29
30
31
32
33
34
35
36
37
38
39
40
41
42
43
44
45
46
47
48
49
50
51
52
53
54
55
56
57
58
59
60
61
62
63
64
65

(a) crushed rock No. 1



(b) crushed rock No. 2



(c) crushed rock No. 3



(d) crushed rock No. 4



(e) crushed rock No. 5



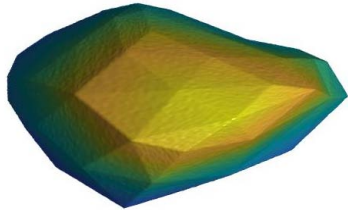
(f) crushed rock No. 6



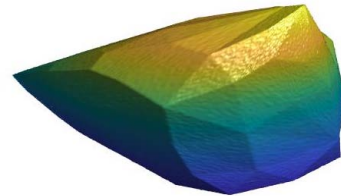
Figure 33: Real crushed-rock-type aggregates: (a) crushed rock No. 1; (b) crushed rock No. 2; (c) crushed rock No. 3; (d) crushed rock No. 4; (e) crushed rock No. 5; (f) crushed rock No. 6.

1
2
3
4
5
6
7
8
9
10
11
12
13
14
15
16
17
18
19
20
21
22
23
24
25
26
27
28
29
30
31
32
33
34
35
36
37
38
39
40
41
42
43
44
45
46
47
48
49
50
51
52
53
54
55
56
57
58
59
60
61
62
63
64
65

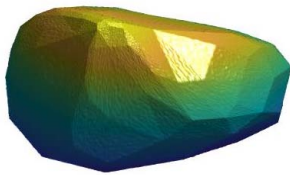
(a) simulated crushed rock No. 1



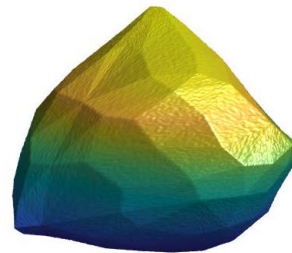
(b) simulated crushed rock No. 2



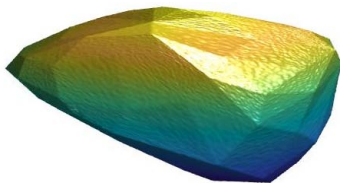
(c) simulated crushed rock No. 3



(d) simulated crushed rock No. 4



(e) simulated crushed rock No. 5



(f) simulated crushed rock No. 6

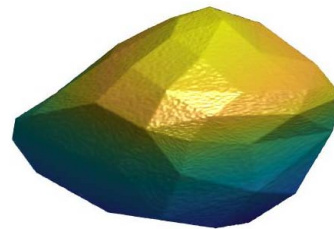


Figure 34: Simulated crushed-rock-type aggregates: (a) simulated crushed rock No. 1; (b) simulated crushed rock No. 2; (c) simulated crushed rock No. 3; (d) simulated crushed rock No. 4; (e) simulated crushed rock No. 5; (f) simulated crushed rock No. 6.

1
2
3
4
5
6
7
8
9
10
11
12
13
14
15
16
17
18
19
20
21
22
23
24
25
26
27
28
29
30
31
32
33
34
35
36
37
38
39
40
41
42
43
44
45
46
47
48
49
50
51
52
53
54
55
56
57
58
59
60
61
62
63
64
65

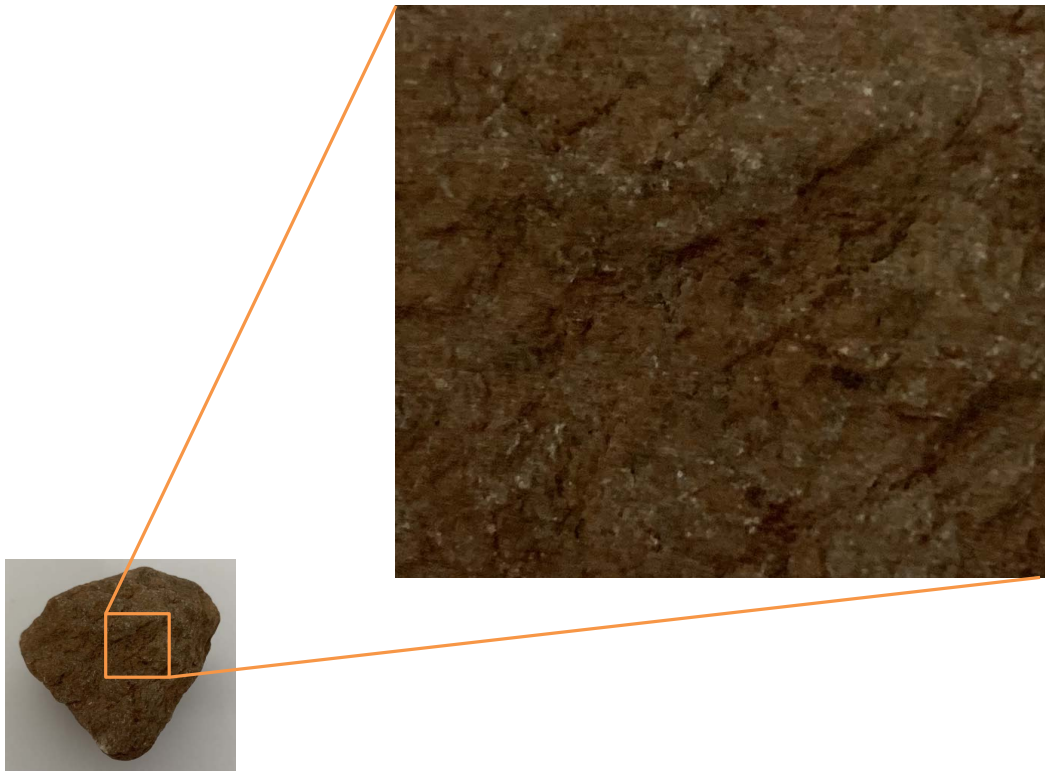


Figure 35: Magnified view of illustrative aggregate microstructure and surface texture.

1
2
3
4
5
6
7
8
9
10
11
12
13
14
15
16
17
18
19
20
21
22
23
24
25
26
27
28
29
30
31
32
33
34
35
36
37
38
39
40
41
42
43
44
45
46
47
48
49
50
51
52
53
54
55
56
57
58
59
60
61
62
63
64
65

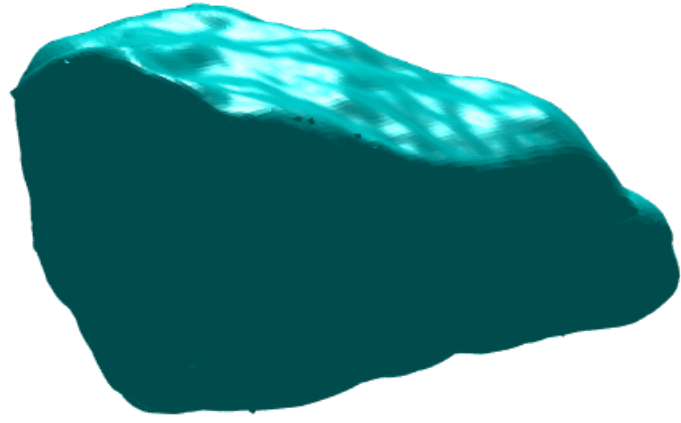
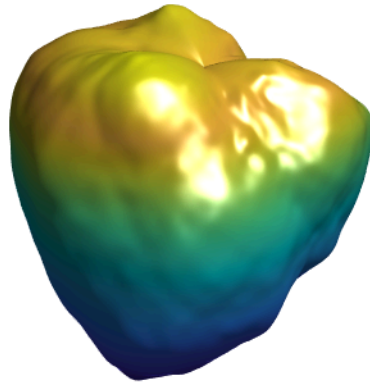


Figure 36: Laser scanned 3D aggregate microstructure with surface texture.

1
2
3
4
5
6
7
8
9
10
11
12
13
14
15
16
17
18
19
20
21
22
23
24
25
26
27
28
29
30
31
32
33
34
35
36
37
38
39
40
41
42
43
44
45
46
47
48
49
50
51
52
53
54
55
56
57
58
59
60
61
62
63
64
65

(a) coarse-scale microstructure



(b) fine-scale microstructure

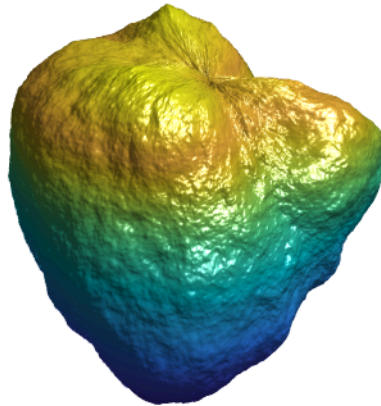


Figure 37: Coarse-scale and fine-scale aggregate microstructure samples with complex surface texture generated by the present approach: (a) coarse-scale microstructure; (b) fine-scale microstructure.

1
2
3
4
5
6
7
8
9
10
11
12
13
14
15
16
17
18
19
20
21
22
23
24
25
26
27
28
29
30
31
32
33
34
35
36
37
38
39
40
41
42
43
44
45
46
47
48
49
50
51
52
53
54
55
56
57
58
59
60
61
62
63
64
65

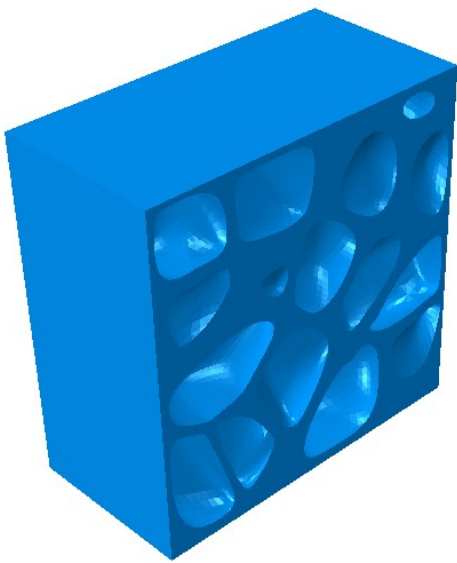
(a1) real RVE with natural gravel



(a2) real RVE with crushed rock



(b1) generated RVE with natural gravel



(b2) generated RVE with crushed rock

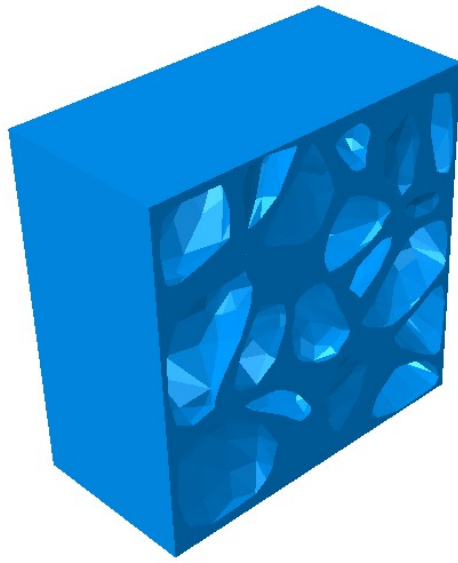
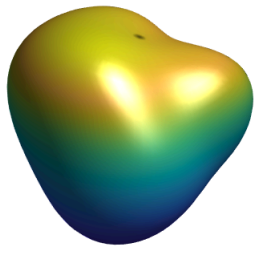


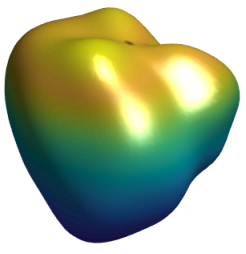
Figure 38: Comparison of computationally generated cementitious RVE microstructures to real cementitious RVE microstructures: (a1) real RVE with natural gravel; (a2) real RVE with crushed rock; (b1) generated RVE with natural gravel; (b2) generated RVE with crushed rock.

1
2
3
4
5
6
7
8
9
10
11
12
13
14
15
16
17
18
19
20
21
22
23
24
25
26
27
28
29
30
31
32
33
34
35
36
37
38
39
40
41
42
43
44
45
46
47
48
49
50
51
52
53
54
55
56
57
58
59
60
61
62
63
64
65

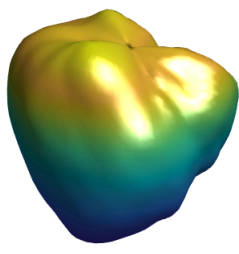
(a) the approach in [16–20] (5 terms of SH series)



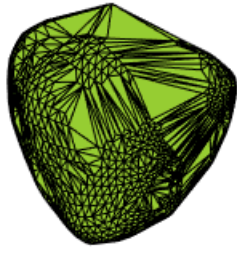
(b) the approach in [16–20] (10 terms of SH series)



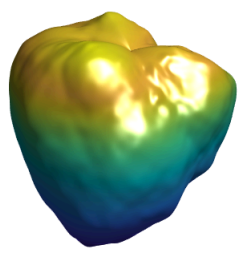
(c) the approach in [16–20] (50 terms of SH series)



(d) the alpha shape approach [23]



(e) coarse-scale microstructure by the present approach



(f) fine-scale microstructure by the present approach

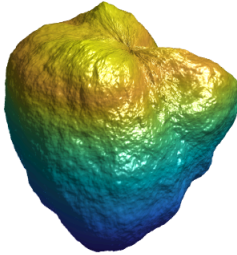


Figure 39: Comparison of the aggregate microstructure generated by the present method and other important contemporary methods: (a) the approach in [16–20] (5 terms of spherical harmonic series); (b) the approach in [16–20] (10 terms of spherical harmonic series); (c) the approach in [16–20] (50 terms of spherical harmonic series); (d) the alpha shape approach [23]; (e) coarse-scale microstructure by the present approach; (f) fine-scale microstructure by the present approach. Note that in the subtitles of the figure, SH stands for Spherical Harmonic.

Declaration of interests

The authors declare that they have no known competing financial interests or personal relationships that could have appeared to influence the work reported in this paper.

The authors declare the following financial interests/personal relationships which may be considered as potential competing interests: